Spring 2023

Nondestructive Evaluation of Structural Defects in Concrete Slabs

Ehsanul Kabir

NONDESTRUCTIVE EVALUATION OF STRUCTURAL DEFECTS IN CONCRETE SLABS

by

EHSANUL KABIR

(Under the Direction of Saman Hedjazi)

ABSTRACT

Nondestructive testing (NDT) is a reliable method for determining the structural integrity of new and old construction and understanding the condition of structural defects. It is widely acknowledged that the interpretation of nondestructive evaluation (NDE) has a significant impact on the reliability and consistency of this technology. However, NDT data acquisition remains subjective and heavily dependent on the operator's knowledge and expertise. As a result, there are still issues to be resolved regarding the imaging and diagnostic procedures for NDT-based concrete inspection. NDT methods such as ground penetrating radar (GPR), and impact-echo (IE), have been extensively used to inspect concrete bridges for damage and deterioration. In this study, concrete slabs were investigated in a laboratory setting with simulated structural defects such as corrosion, delamination, honeycomb, and voids. To validate the accuracy and robustness of the two NDT methods, defects were embedded closely (ranging from 1 to 5 inches) and superimposed in two different layers for the same specimen. GPR B-scan (line scan) radargrams demonstrated hyperbolic shapes for voids and corroded rebars, whereas delamination was identified by a hollow strip pattern. GPR C-scan (area scan) data was used to calculate the size (length, width, and thickness) of delamination simulated by polystyrene sheets. The results showed an accuracy of 80% in predicting the thickness of delamination. GPR, however, did not detect delamination for objects smaller than 8 inches in size due to the dense meshing. The amplitude data from GPR A-scans (amplitude vs depth) were used to calculate the depth of a defect. Statistical measures exhibit a high degree of agreement between the depth measured by GPR and the actual depth of a defect. The IE method uses elastic waves to propagate through concrete for identifying the embedded defects. The interpretation of IE data involved post-processing of reflected signals in the time-domain and frequency-domain modes. The simulated structural defects did not show any discernible trend in time-domain data. However, defects were detected using IE thickness data from the peak frequency spectrum. The frequency-domain IE data was validated by comparing it to GPR data for similar concrete specimens.

INDEX WORDS: Concrete, Ground penetrating radar, Impact-echo, Nondestructive evaluation, Nondestructive testing, Structural defects

NONDESTRUCTIVE EVALUATION OF STRUCTURAL DEFECTS IN CONCRETE SLABS

by

EHSANUL KABIR

B.S., Ahsanullah University of Science & Technology, Bangladesh, 2013

M.S., Georgia Southern University, 2023

A Thesis Submitted to the Graduate Faculty of Georgia Southern University

in Partial Fulfillment of the Requirements for the Degree

MASTER OF SCIENCE

STATESBORO, GEORGIA

NONDESTRUCTIVE EVALUATION OF STRUCTURAL DEFECTS IN CONCRETE SLABS

by

EHSANUL KABIR

Major Professor:	Saman Hedjazi
Committee:	Hossein Taheri
	L. Stetson Rowles

Electronic Version Approved:
May 2023

DEDICATION

This thesis is dedicated to my father, who had the chance to pursue a graduate degree in the United States during the 1980s but was unable to do so due to a tragic event. I am grateful for the opportunity to pay tribute to him through my academic accomplishments.

ACKNOWLEDGEMENTS

I would like to thank my thesis advisor Dr. Hedjazi for his dedicated support and guidance during my graduate studies at Georgia Southern. I would also like to thank my committee members for their insightful comments and suggestions. Furthermore, I would like to thank the undergraduate research team (Charles, Gabi, John, and Kristin) for their help with sample construction.

TABLE OF CONTENTS

LIST OF TABLES

LIST OF FIGURES

LIST OF ABBREVIATIONS

ASTM	American Society for Testing and Materials
Dk	Dielectric Constant (ε_t)
DOT	Department of Transportation
DT	Destructive testing
EM	Electromagnetic
GDOT	Georgia Department of Transportation
GP	Proceq GPR Mobile App
GPR	Ground penetrating radar
NDT	Nondestructive testing
ns	Nanoseconds
RC	Reinforced concrete

CHAPTER 1

INTRODUCTION

Deterioration of concrete is a common phenomenon on bridge decks. Bridge engineers around the world are more concerned about the subsequent deterioration of concrete decks when it comes to bridge maintenance and rehabilitation. Various structural defects and environmental factors can cause the deterioration of a concrete deck during its design life. Some examples of structural defects in concrete are blistering, corrosion, cracking, debonding, delamination, efflorescence, honeycomb, scaling, spalling, voids, etc. These defects have a negative effect on the required strength of concrete, which can lead to reduced serviceability and/or an unexpected collapse of the bridge deck (Nelson et al., 2021). Concrete deck deterioration can be either real or apparent. Because the underlying concrete is not accessible for direct inspection, nondestructive testing (NDT) methods can be used to determine the deteriorated areas of concrete bridge decks throughout their service lives. Hence, the proposed study aims to identify structural defects in concrete slabs using various NDT techniques to provide a quantitative prediction of concrete deterioration in bridge decks.

Purpose of this study

Nondestructive evaluation (NDE) techniques such as ground penetrating radar (GPR) and impact-echo (IE) have gained popularity for concrete deck inspection due to their rapid data collection and in-situ assessment capabilities (Benedetto et al., 2017; Kang et al., 2017; and Wharton et al., 2017). However, GPR and IE studies have primarily focused on big data processing for corrosion mapping/modeling based on bridge condition surveys, ignoring the importance of experimental investigation of concrete structural defects for identifying bridge deck deterioration. Furthermore, data collection using these NDT methods is highly dependent on the user's perception and experience (Tesic et al., 2021; Dawood et al., 2020; and Zatar et al., 2020) On the other hand, the interpretation of NDT results has a significant impact on the reliability and consistency of the technology (Rashidi et al., 2020) The

purpose of this research to identify the artificially embedded structural defects in experimental concrete slabs using NDT methods.

Goals and Objectives

The objectives of this study are: 1) to identify the artificial defects embedded in experimental concrete slabs using GPR; 2) to identify the artificial defects embedded in experimental concrete slabs using IE; and 3) to compare the scan results from both NDTs to validate the identification of concrete slab deterioration. It will be easier to use and apply the two NDT methods under consideration for in-situ application if accurate measurements of intentionally embedded defects are obtained. Understanding the application of these NDE techniques will also help to determine potential deteriorated areas in bridge decks during inspection.

Hypothesis

NDT methods such as GPR and IE have already been used effectively to evaluate concrete structures for deterioration. Nonetheless, the interpretation of NDT results for determining structural defects can be subjective due to multiple variables. If real-life structural defects are artificially embedded in concrete slabs, both GPR and IE techniques can successfully identify them.

CHAPTER 2

LITERATURE REVIEW

Corrosion of the reinforcing steel in a concrete deck is the primary cause of various near-surface defects (Kuruppu et al., 2022 and Aktan et al., 2003). Several factors can cause rebar corrosion. Concrete bridges often have a reinforced concrete (RC) deck with no asphalt. Construction of such bridges take less time and money; however, the deck is more vulnerable to corrosion of the embedded reinforcement because it is only protected by the concrete cover or a corrosion-resistant top layer on the deck surface. As a result, deicing salts, which are used to prevent snow and ice on bridge decks, easily penetrate concrete and cause rebar corrosion over time (ASTM, 2008). In addition, the presence of chloride ions in concrete mixture can cause chloride-induced corrosion which is usual in RC decks (Chen and Qiao, 2015). Corrosion of rebars frequently results in concrete delamination. Delamination can cause any topcoat on the concrete surface to separate. This allows water and moisture to penetrate and disperse through the pores in concrete (Caputo et al., 2017). Long-term corrosion of reinforced steel can result in debonding between the steel reinforcement and concrete, and ultimately exposing the rebars to the environment (Dinh and Gucunski, 2021). This often leads to honeycomb in concrete, which can severely damage or deteriorate the adjacent deck. When visible structural defects or damage are present in the concrete deck, the cost of repairs and maintenance increases. Moreover, the service life expectancy of the bridge deck is reduced (Drobiec et al., 2010). As a result, concrete bridge decks must be inspected for structural defects on a regular basis to ensure the structural integrity of the bridge.

Destructive testing (DT), semi-destructive testing, and nondestructive testing (NDT) methods are used in evaluating defects of concrete bridge decks (Sultan and Washer, 2018). The applicability of DT to existing bridge inspection is typically limited because it normally involves the demolition of samples or structural components to obtain results. Semi-destructive testing, on the other hand, requires extrusion of samples from structural elements, which may result in localized degradation of service properties and subsequent repair. However, NDT is an ideal method for bridge inspection in

many cases because it does not require any sample intrusion or demolition and can be used repeatedly on the same structural components both during construction phase and for the duration of their service life (Sham et al., 2017).

Several NDT methods have been developed to assess the structural integrity of concrete decks without compromising bridge serviceability. Among NDT techniques, GPR is an advanced technique with the potential for effective deployment at highway speeds (Abouhamad et al., 2017). The number of GPR inspection studies conducted on RC structures and bridges to identify problems and propose solutions has increased over the last decade (Benedetto et al., 2017 and Trung et al., 2018). Wong et al. evaluated concrete delamination in RC slabs due to rebar corrosion in a controlled environment and identified the corroded areas using GPR. The authors reported that the amplitude of reflection signal from the corroded rebars was 30% higher than plain rebars. When corrosion defects in concrete slabs are not visible on the surface, this research suggested that the maximum amplitude of the signal reflected from the rebars is a useful gauge for integrity assessment of bridge decks (Wong et al., 2018).

In contrast to the conventional random sampling of cores used for structural diagnosis, a case study on pier structures at Macau Ferry terminal in Hong Kong demonstrated the advantages of using a GPR survey to avoid missing important defects or oversampling non-defective areas (Hong et al., 2015). GPR measures physical properties based on the contrast of electrical and dielectric properties when a case-specific depth range and resolution are met (Shaw et al., 2005 and Lai et al., 2013). This dielectric attenuation can alter the wave parameters in the vicinity of a corroded steel bar in an RC deck, which can be easily detected using GPR (Benedetto, 2013). However, the data collected using GPR method still faces challenges. There are no specific guidelines regarding the impact of background noise sources on GPR data. The American Society for Testing and Materials (ASTM) proposed using GPR evaluation to assess the condition of concrete bridge decks in three scenarios: (i) asphaltic concrete wearing surfaces on bridge decks, (ii) bridge decks with Portland cement concrete overlay, and (iii) bridge decks that do not have an overlay (ASTM, 2011).

There is a gap in the literature regarding GPR's ability to detect various types of near-surface defects in concrete. The scan results of a GPR evaluation can show whether rebar or concrete deterioration exists at or above the top layer of the reinforcement bar. However, Hong et al. demonstrated that when collecting GPR data perpendicular to the bottom reinforcing bar with the antenna directly over and parallel to the top bar, the top reinforcing bar partially reflects the incident radar wave before it is reflected off the bottom bar (Hong et al., 2012). As a result, the bottom bar's reflection amplitude is diminished, resulting an incorrect assessment of the bridge deck (Lai et al., 2011). Consequently, the potential influence of GPR equipment orientation for data collection on two reinforcing layers remains uncertain. Previous studies used differently polarized antennas to provide information about rebar location. Soldovieri et al. (2006), on the other hand, proposed an inverse scattering approach to accurately identify the rebar location in concrete structures (Soldovieri et al., 2006). The presence of reinforcement corrosion or concrete damage in the form of delamination or cracking was determined based on the interpretation of the reflected GPR signals. However, the post-processing of the collected data to distinguish between sound and deteriorated concrete deck is still being debated (Zanzi et al., 2013 and Ahmad & Bond, 2018).

Nondestructive analysis of RC bridge decks includes three types of inspections: geometry and orientation (concrete cover, rebar alignment and spacing, member thickness); durability (carbonation, chloride content, corrosion, crack, delamination, moisture content); and strength (strength of concrete, modulus of elasticity of steel) (ASTM, 2007 and Cotic et al., 2015). GPR is best suited for checking the geometry and orientation of reinforcement, as well as the durability of concrete, but it is not suitable for strength testing (Hasan, 2012). GPR has been shown to react to corrosive environments on bridge decks, according to some research (Lai et al., 2011). Research into using GPR to detect corrosion and delamination in concrete is worthwhile due to the high dielectric contrast between air and concrete, as well as other benefits such as quick data collection and 3D imaging capability (Clem et al., 2013). It is critical to conduct extensive research on bridge inspection with GPR for effective concrete deck maintenance and repair to save costs and ensure the designed service life of bridges.

While GPR can provide useful information, data collection and analysis remain dependent on the user's experience and skills. Furthermore, GPR data is heavily dependent on variables such as moisture and concrete age (Oikonomopoulou et al., 2022). Infrared thermography (IR), on the other hand, has been shown to be a reliable NDT method for detecting near surface defects in concrete. Unfortunately, ambient temperature can have a significant impact on the collection and analysis of IR data (Klimenko et al., 2021 and Wong & Subramaniam, 2019). The use of ultrasonic testing (UT) to inspect concrete bridges for structural defects has proven to be effective. However, due to the need for access to both faces of the member for ultrasonic wave propagation, UT can only be applied to small concrete members (Kot et al., 2021 and Xiao et al., 2015). Table 1 presents a brief comparison of several NDT approaches. The IE testing method has a high potential for detecting defects in concrete structures regardless of moisture content, ambient temperature, or concrete age (ASTM, 2022 and Xu et al., 2020). It is a point-wise inspection method that uses the transient vibration response of a solenoid impactor to record the response of a structure at various locations. But it has been argued that using raw IE signals for in-situ inspection of concrete structures contains unidentified signals that cannot be taken into account in the calculation of IE data (Lee et al., 2021; Pratt et al., 1992; and Schubert et al., 2008). Therefore, using IE data without interpreting them could be difficult. It is critical to understand the characteristics of IE signals with simulated structural defects in a laboratory setting for concrete slabs.

Previous researches have shown that IE test can be used to evaluate horizontal cracks in concrete both in-situ and in a laboratory setting (Zhu et al., 2018). IE is a reliable NDT approach that has been demonstrated to be effective in detecting delamination in bare (no asphalt over-lay) concrete bridges (Coleman & Schindler, 2022; Hu et al., 2022; and Wong et al., 2018). Experiments were carried out to assess the transient IE response of concrete beams of various sizes and aspect ratios (Kee et al., 2012). The IE approach was effectively used to find defects, flaws, inclusions, and voids on the concrete piers of a highway project using on-site measurements (Matsuyama et al., 2010). Dawood et al. investigated the effectiveness of using IE approaches to detect the degree and location of cracks and local damage in structural elements on a Jetty bridge construction (Dawood et al., 2013). Based on IE testing principle, a

new detection system for condition assessment was developed for checking defects at Gyeongbu Express Railway track-bed. According to the findings of this study, IE can be used for condition monitoring to check cavities beneath the concrete slab track (Park et al., 2018). IE techniques were used to understand the residual durability attributes and a framework was built using microstructural and thermal analyses (Aseem et al., 2019). The IE testing technique has been successfully used to detect delamination in bridge decks, voids in grouted PT ducts, voids behind tunnel lining, structural integrity testing of fire damaged concrete elements (Chaudhary, 2013). ASTM C1383 was adopted to officially regulate the approach for measuring concrete deck thickness using the IE method (ASTM, 2004). The IE method was used to detect structural damage in offshore structures (Ekenel & Myers, 2004 and Zein & Gassman, 2010).

Table 1: Comparison of NDT methods for detecting bridge deterioration

NDT	Advantages	Limitations
GPR	Data collection is both quick and detailed.	GPR can only detect contrast between the object and its surroundings, not the composition of the object.
IE	Metallic objects reflect less acoustic waves than EM waves such as GPR, allowing objects behind rebar visible.	To detect the relatively large wavelength, test components with a large diameter are required.
IR	Sensitive to mapping surface defects.	Poor resolution on thick sections.
UT	Internal defects can be detected irrespective of the thickness of the specimen.	Defect may be missed if not in the path of the ultrasonic signal.

This study aims to identify the artificial structural defects embedded in experimental concrete slabs using two commercially available NDT techniques such as, GPR and IE. This study will propose guidelines for detecting, mapping, and visualizing potential deterioration of concrete based on

experimental data, which could aid in comprehending the use of GPR and IE methods for bridge inspection. A comparison between the scan results from both NDTs will be presented to validate the identification of concrete slab deterioration.

CHAPTER 3

METHODOLOGY

Concrete slabs with embedded structural defects were designed and built in a laboratory setting using objects commonly used in the construction of real-life structures (e.g., buildings, bridges, etc.), in accordance with previous NDT inspection research (Drobiec et al., 2019; Janku et al., 2019; and Luo et al., 2020). Four concrete slabs with artificial defects and one control (or witness) slab with no defects were poured. During the concrete pour, water was adjusted to match the moisture content and absorption capacity of the aggregates, and a w/c ratio of 0.45 was maintained for all concrete slabs. The average 28-day compressive strength was 25.8 MPa (cylinder test). The specimens had uniform dimensions of 3 ft. × 3 ft. (length × width) with thicknesses of either 5 inches or 5.5 inches. The width-to-thickness ratio for the specimens was greater than 5.0 in order to prevent noise caused by wave reflections from the slab edges (Yehia et al., 2007). Defected specimens were split down the middle to implant defects in two sides. For objects embedded after a 2-inch layer of concrete is poured from bottom was labeled as 'Side A'. Therefore, the opposite side is labeled 'side B' for objects placed following a 4-inch layer of concrete pour from the bottom surface. There are a few exceptions, which are briefly discussed in Table 2.

Table 2: Summary of model concrete slabs with structural defects

Specimen ID	Simulated Defect(s)[c]	Additional Description
S1[a]	–	Control (or witness) slab shown in figure 1.
S2[b]	DL	Polystyrene sheets of 3/8 in. (0.95 cm) thick were placed in two layers to simulate DL. The first sheet (3 ft. × 3 ft.) was placed at a depth of 3.5 in. beneath the top face of the panel (Figs. 2a & 2c). The second sheet (1.5 ft. × 1.5 ft.) was placed 2.5 in. below the top on side "A" (Figs. 2b & 2d). After the formwork

		was removed, the edges of the slab revealed both sheets. Therefore, the exact depth is known.
S3[b]	DL	Four different types of small DL targets were embedded inside the concrete slab in two layers using the same Polystyrene sheet (3/8 in. thick). Figures 3a-3d show the horizontal distribution and dimensions of the targets for both sides. The precise location and depth of the DL targets could not be maintained during the concrete pour.
S4[a]	H, V	On side A, three plastic bottles (Aquafina 12 fl. oz water bottles, height = 7 in., and width or diameter = 2.5 in.) and three latex balloons (4 in. diameter) were placed at the 2 in. layer from bottom to simulate voids (Fig. 4). The bottles were partially filled with concrete smudge to keep their positions, but they float to the surface. However, their positions (locations) were retained during the finishing of concrete pour according to the drawing (Fig. 4c). The balloons, on the other hand, were filled with water to hold their positions in concrete. However, the pink balloon in the center was popped during the concrete pour. The other two balloons (blue and yellow) float to the surface and pop once the concrete hardens (within 24 hours of slab casting). This results in two 4 in. diameter voids on the top surface of the concrete slab. On side B, the top surface of the slab was fabricated with a honeycomb measuring 2-3 inches (5.1-7.6 cm), as shown in figure 4e. In addition to that, 1 ft. (30.5 cm) long ½ in. PVC pipes with an inner diameter of ¼ in. (0.64 cm) were placed in two layers to simulate voids. The details are shown in figures. 4c and 4d.
S5[b]	C	In this case, side B was employed as control (or witness) slab since it has no defects.

		On the opposite side A, two No. 4 (diameter = 12 mm or 0.50 in.) and one No. 3 (diameter = 10 mm or 0.375 in.) bars were placed. ASTM standard rebars were used. The No. 3 bar on the slab was in the corner. To maintain uniform spacing between the rebars and clear cover from the bottom of the slab, concrete blocks of 3×3 inches (for spacing) and 2×2 inches (for cover) were used respectively. The blocks were placed and secured with rebars from the bottom. To simulate corrosion, corroded rebars were used.
[a] slab thickness of 5 inches [b] slab thickness of 5.5 inches [c] Corrosion (C), delamination (DL), honeycomb (H), voids (V)		

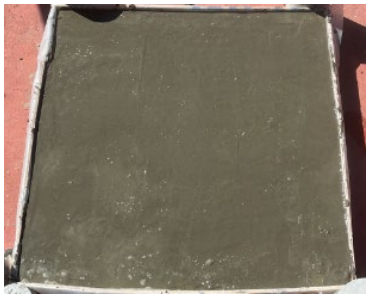

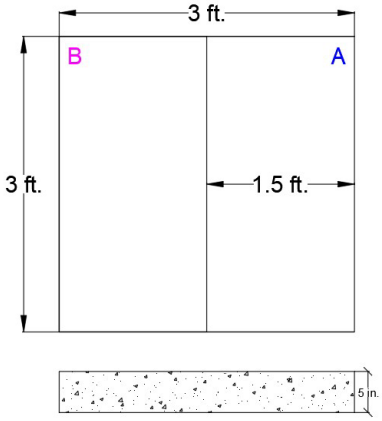

Figure 1: Control or witness slab

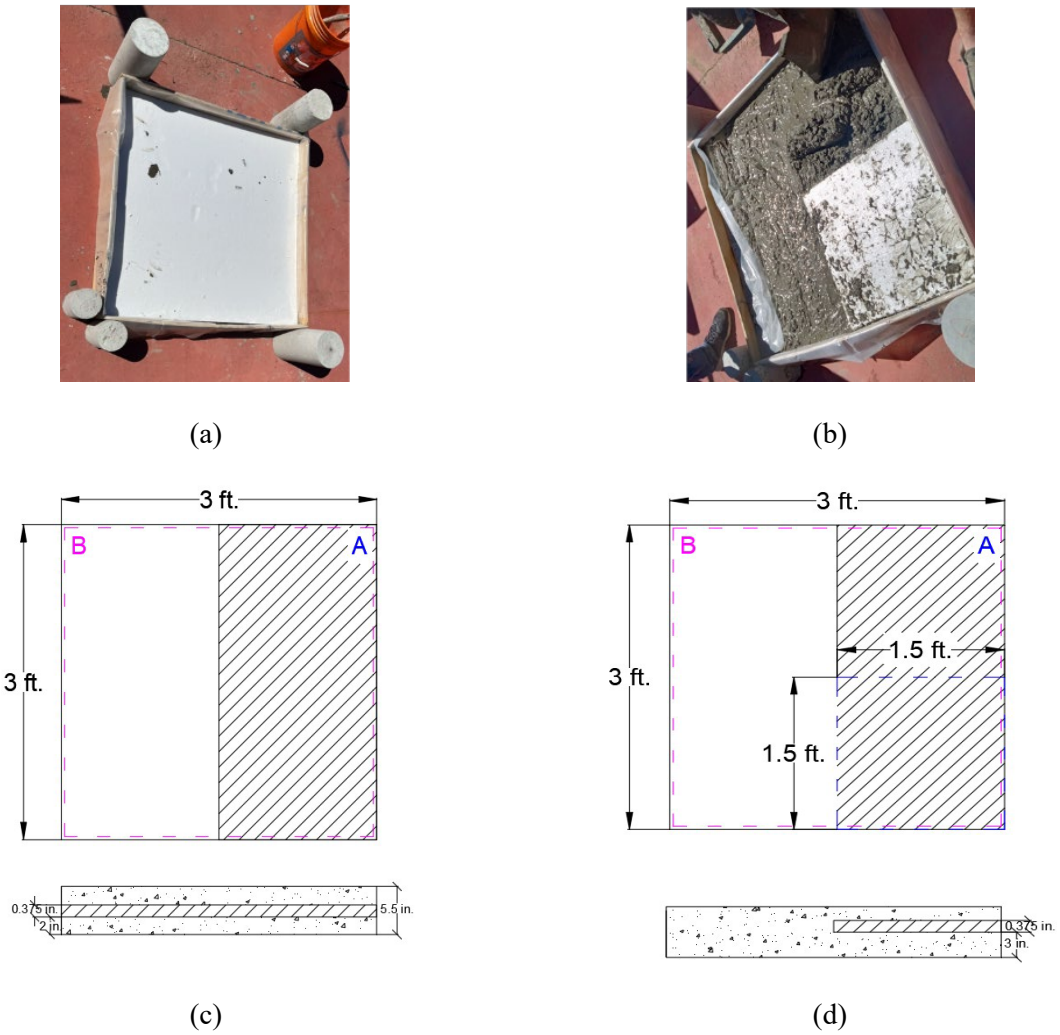

Figure 2: Specimen S2 embedded with polystyrene sheets to simulate delamination

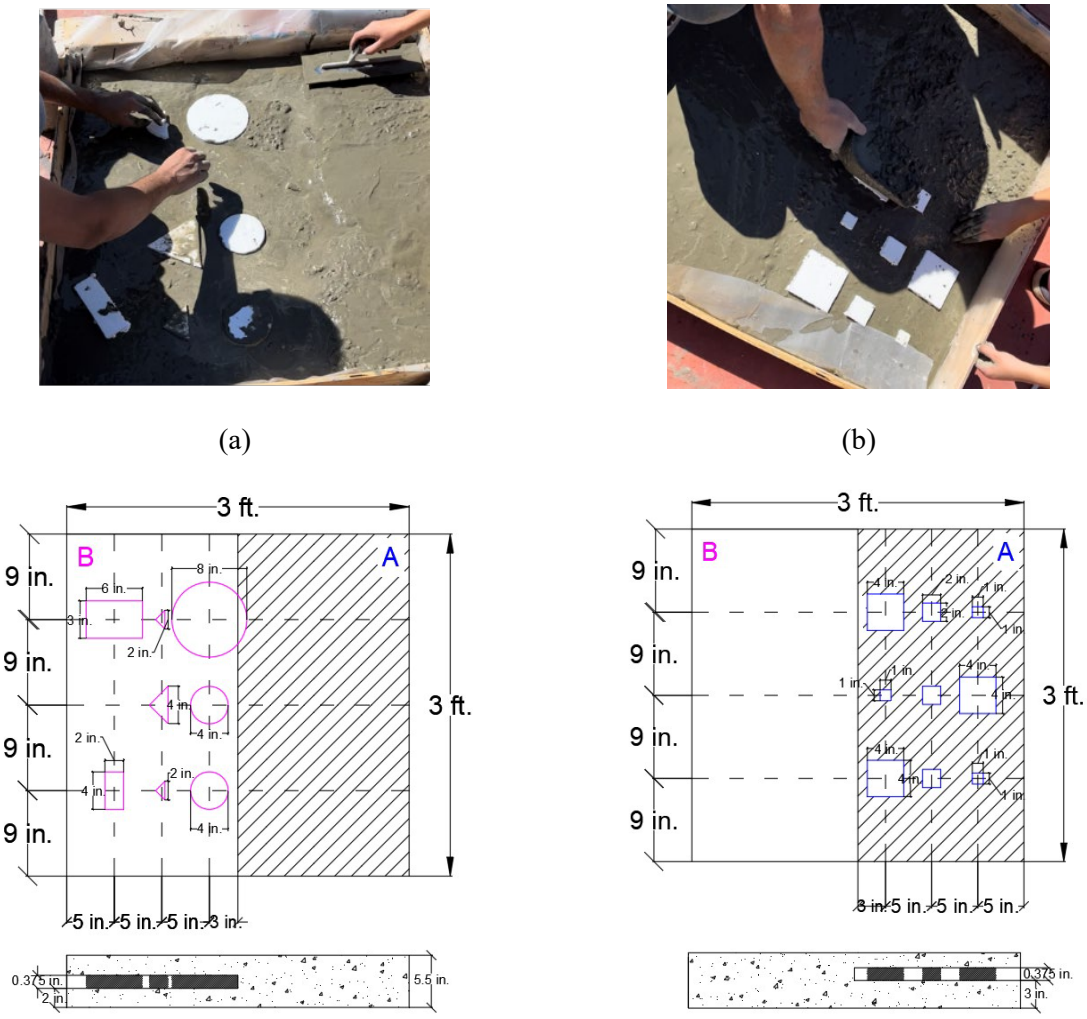

Figure 3: Specimen S3 implanted with small delamination targets (polystyrene blocks)

(a)

(b)

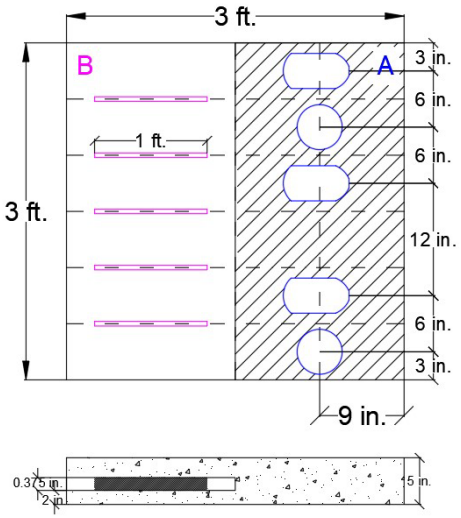

(c)

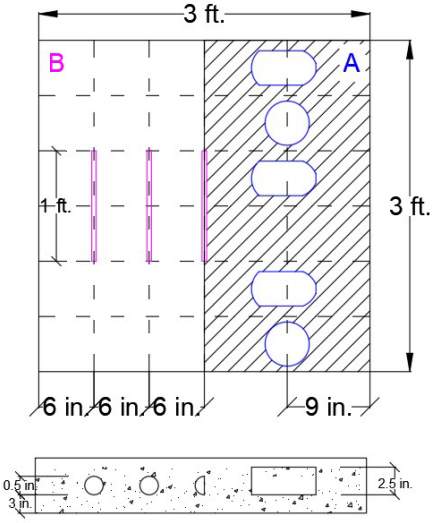

(d)

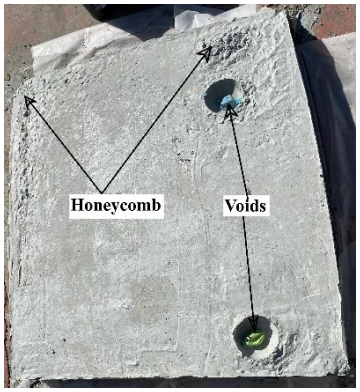

(e)

Figure 4: Specimen S4 representing honeycomb and voids

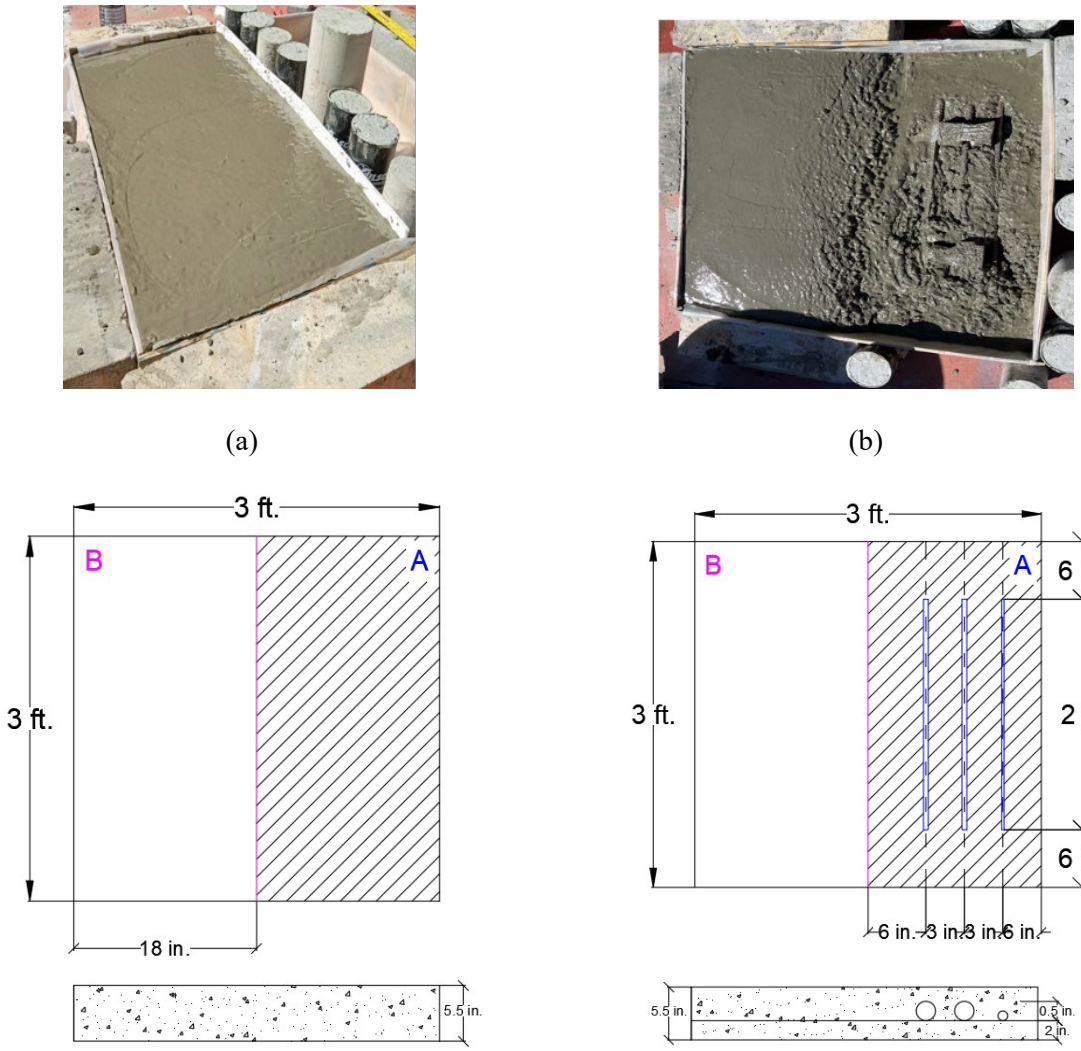

Figure 5: Specimen S5 embedded with corroded rebars

Working Principles of GPR

GPR is a noninvasive geophysical locating method that generates images of subsurface features using electromagnetic (EM) waves. In general, a GPR equipment used for nondestructive evaluation (NDE) consists of five major components: a transmitter antenna, a receiver antenna, a radar control unit, a display device, and adequate data storage (ASTM, 2019). However, a single antenna can serve as both a transmitter and a receiver. The portable concrete GPR used in this study, the Proceq GP8000

from Screening Eagle Technologies (USA), for example, employs a monostatic (or transceiver) ground-coupled antenna system for transmitting and receiving EM waves (Fig. 6). It uses the stepped-frequency continuous-wave (SFCW) radar technology to generate modulated frequencies ranging from 200 – 4000 MHz with a penetration depth of 31.5 inches (80 cm). The waveform of SFCW radar is generated by transmitting a series of single-frequency waves separated by ΔF hertz. The amplitude and phase of the received data are sampled and recorded at each frequency. The data is then transformed into the spatial domain using the Inverse Discrete Fourier Transform (IDFT) in most implementations which produces a synthesized pulse (0-20 ns) (Langman and Inggs, 2001).

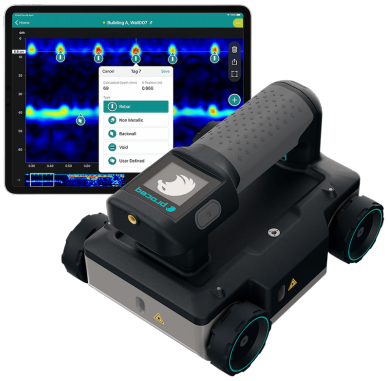

Figure 6: Proceq GP8000 GPR unit

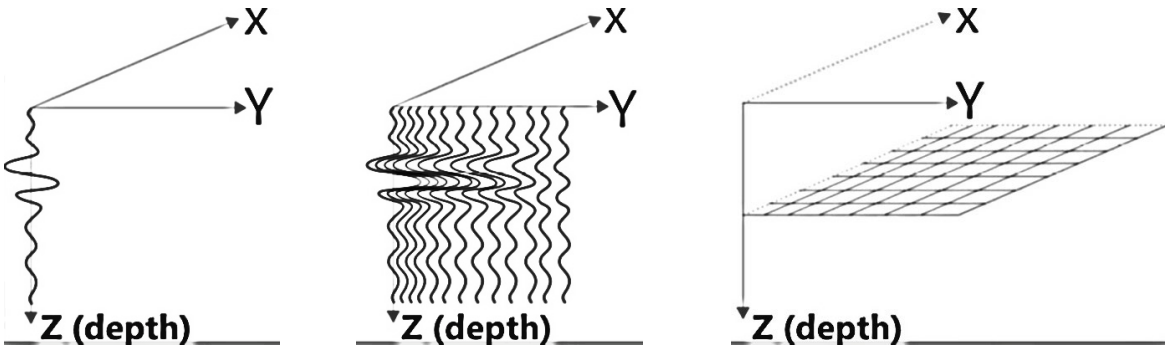

(a) A-scan (b) B-scan (c) C-scan

Figure 7: Signal imaging of GPR radar

The GP8000 probe has a post processing mobile app, Proceq GPR App (GP), which records, processes, and displays the collected GPR data when connected to the probe's wireless network. Once the probe receives GPR signals, they are stored and displayed in the user interface (UI) for meaningful representations. GPR data can be displayed in three ways: one-dimensional (A-scan), two-dimensional (B-scan), and three-dimensional (C-scan), shown in figure 7. The three different visualization modes can obtain three different types of information. The A-scan is a single radar trace along the depth axis, the B-scan is a collection of consecutive single radar traces collected along a certain scanning direction, and the C-scan is a collection of B-scans extrapolated at a specific spacing along the depth axis (Tosti and Ferrante, 2020). For a reliable GPR interpretation, the data must be collected accurately. The most common cause of errors in data acquisition is due to wrong or inappropriate settings of parameter. This may result in inconsistent, blurry, or clipped traces of the visualization during the inspection. For data collection, the GP app has two major settings: (i) Measuring Presets, and (ii) Image Processing. The appendix contains detailed information on the GP app settings for data collection with GPR.

Working Principles of IE

Impact-generated stress (sound) waves are used in IE testing. These elastic waves travel through the structural members and are reflected by the external surface and/or internal defects as shown in figure 8. Due to the mechanical impact, three types of elastic waves propagate (or reflect) at the same time: two types of body waves (P-waves and S-waves) and surface-guided waves (e.g., Lamb and Rayleigh surface waves). Theoretically, an infinite set of non-propagating wave modes (or vibration resonance modes) of the plate-like specimen (slab or wall) is set up by the multiple-reflected and mode-converted body waves guided by the two free surfaces of the test specimen. In practice, a vibration sensor (e.g., a displacement transducer, accelerometer, microphone, etc.) is located close to the impact source to measure the dynamic response of the plate (Sansalone and Carino, 1989). The NDE-360 with IE-1 system from Olson Instruments Inc., USA was used to record the impact response in this study. This IE-1 system typically includes a standard IE test head with an integrated impactor and displacement sensor for sending

and receiving resonant echoes. The NDE-360 platform uses IE cables to connect to the designated IE channel for data acquisition, analysis, and display. The IE tests with the standard test head involve striking the concrete member with an impactor solenoid and measuring the reflected wave energy with a displacement transducer. The IE test head is pressed against the top of the test specimen and held in place while tests are performed at each test point. The resonant echoes of the displacement responses are usually not visible in the time domain, but they are more easily detected in the frequency domain.

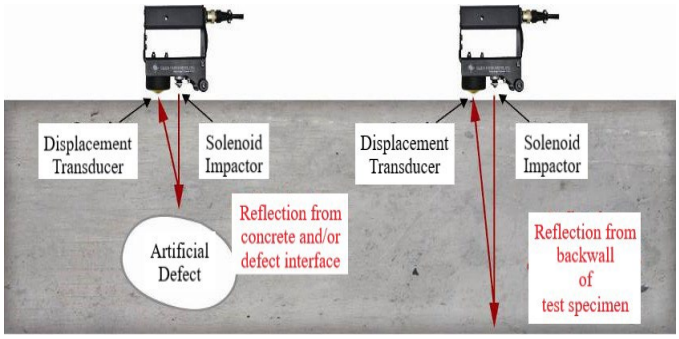

Figure 8: IE test methodology (Lai et al., 2011)

To determine the resonant echo maxima (peak), the amplitude spectra of the displacement responses are calculated using a Fast Fourier transform (FFT). The following equation expresses the relationship between the resonant echo depth frequency peak (f), compression wave velocity (V_p), and echo depth (D):

$$D = \frac{\beta V_p}{2f} \qquad \text{(Equation 1)}$$

where β is a geometric shape factor (Sansalone and Streett, 1997) ranging from 0.945 to 0.957 for concrete (Lee et al., 2020) and is dependent on the Poisson's ratio of concrete (Gibson and Popovics, 2005). For the purposes of this study, β is considered 0.96 as specified by the manufacturer for a slab or wall shape (Sansalone and Carino, 1989). To post-process the IE data and perform more detailed analysis, the NDE-360 system includes a data analysis program called Windows WinIE that includes several specialized IE data analysis tools.

Data Acquisition with GPR

The ASTM D4748 – 10 guidelines were followed when collecting GPR data for this study. The data acquisition process employed two different approaches. First, line scans were performed on each specimen. The location of defects (objects) embedded in the concrete slabs was taken into account when determining the scanning direction of the line scans. Two random line scans were performed in both directions on S1. In contrast, for S2, scans were taken in the center of the Polystyrene sheet embedded 4 inches from the slab base. Additionally, for S3 and S4, line scans were taken adhering to the grids, while scans for S5 were taken in the longitudinal and perpendicular directions of the reinforcement. Figures 9a-9e show the direction of line scans for each slab, where L1– L9 represent the numbers of line scans performed during each inspection. Each line scan had a total length (distance) of either 2 ft. or 3ft. (approximately).

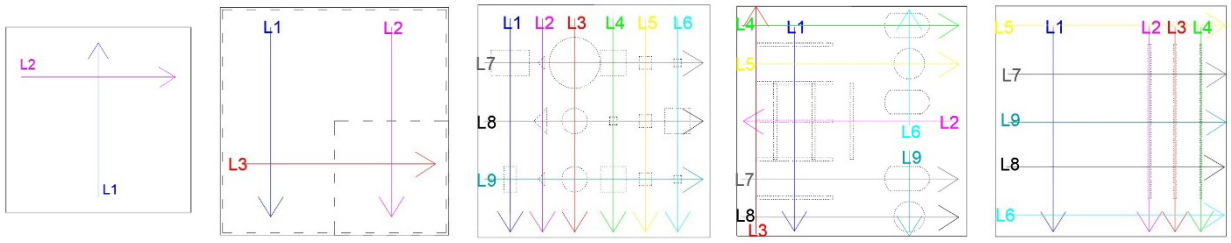

(a) S1 (b) S2 (c) S3 (d) S4 (e) S5

Figure 9: Data collection using line scans

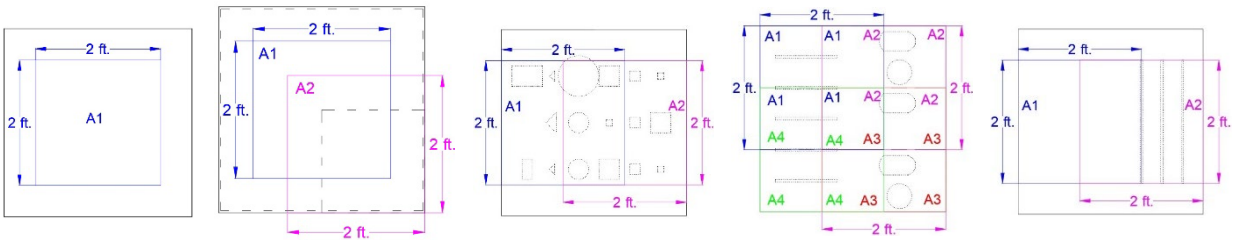

(a) S1 (b) S2 (c) S3 (d) S4 (e) S5

Figure 10: Data collection using area scans

Second, each specimen was subjected to area scans using the standard 2 ft. × 2 ft. grid sheet included with the GP8000. Two grid sizes were used: (i) a 4 in. × 4 in. grid size that divided the 2 ft. × 2 ft. sheet area into 36 zones, and (ii) a 2 in. × 2 in. grid size that divided the 2 ft. × 2 ft. sheet area into 72 zones. The latter was only employed for S3 and S5 (side A). Scanning areas in the concrete slabs for area scan were selected to accommodate potential zones of defects (objects). For S4 area scans, the grid sheet was placed at all four corners. In contrast, grid sheet was placed at the edge of the slab covering the defects (objects) in S3 and S5, as shown in figure 9. Grid sheet was positioned in the middle of the slab for S1 and S2. For S2 (side A), where the Polystyrene sheet was placed, another scan was taken. A1, A2, A3, and A4 represent the number of area scans taken during each inspection as shown in figures 10a-10e. To eliminate data collection errors, each dataset was confirmed by three consecutive scans for both line and area scan.

There are three pointers (red color) around the GP8000 probe when the device is turned on and connected with the GP app. The distance between the center of the wheel and the red pointer is 3.5 in. The probe starts collecting data by taking the red pointer as the starting point. However, the exact location of an object was obtained by considering the mid-point of the three pointers (i.e., the center of the equipment). This has been validated by taking measurements on one slab using a measuring tape and watching the scan data on the iPad screen. No error was found on data acquisition for distance (length) with GP8000, and the measurements taken.

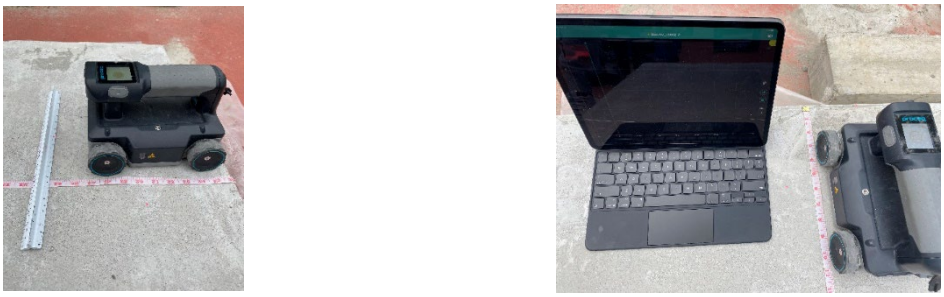

Figure 11. Calibration of equipment

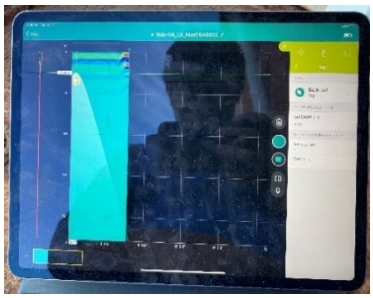

Figure 12. Calibration of dielectric constant

For example, the GP8000 was moved 10 in. from its initial position with a tape at 28 in. at the center of the front wheels (Fig. 11). The scan length measured by tape and the line scan data displayed in the GP app were comparable. When the equipment was observed for a 'Superline Scan', similar results were obtained.

Table 3: Values of Dk, Humidity, and Temperature during Data Collection

	Collected Data			Range of Data	
	7 days	14 days	28 days		
Dk of Concrete (Obtained from equipment)	7.1	6.7	6.5	Dk for dry concrete = 4 to 9 (Zhu et al., 2018) Dk for normal concrete = 4 to 10 (Coleman and Schindler, 2022)	
Relative Humidity	45%	35%	28%	18-55%	Data for the month of October 2022 in Statesboro, GA, United States
Average Temperature	81^0F	79^0F	78^0F	74-80^0F	

To calibrate the Dk, the user must manually set 'Depth' in the GP app while performing line scan. This can be accomplished by selecting the 'Tag' option from the GP app, positioning the cursor

at the slab thickness level in the screen, and selecting ‘Backwall’ as the object. The user can manually enter the depth of the slab in the ‘Set Depth’ option, and the software will automatically calibrate the Dk for the material. A hyperbolic shape will appear on the screen, indicating that the calibration was successful as shown in figure 12. Table 3 shows the Dk for the studied slabs as well as the range of Dk for concrete. Given that all the measured values are within the typical range for concrete, the calibration can be confidently stated to be accurate across all the concrete slabs.

Table 4: Calibration of concrete velocity

Specimen ID	Thickness (in)	Average concrete velocity after calibration (ft./s)
Slab 1	5.5	10231
Slab 2	5.5	9463.4
Slab 3	5.0	8138
Slab 4	5.0	14183

Data Acquisition with IE

When collecting IE data for this study, the ASTM C1383 – 15 guidelines were followed (ASTM, 2022). The data acquisition process used a grid system of transverse and lateral gridlines that were marked on the top surface of the concrete slabs as shown in figure 13. For this study, three grid systems were selected for the concrete slabs, covering the entire defect or defect areas, and excluding the boundary edges. The side ‘B’ of the tested specimen is shown by a hatched section. Before beginning data recording, the data acquisition parameters were manually adjusted in the NDE-360 system to meet the measurement requirements (Figure 14).

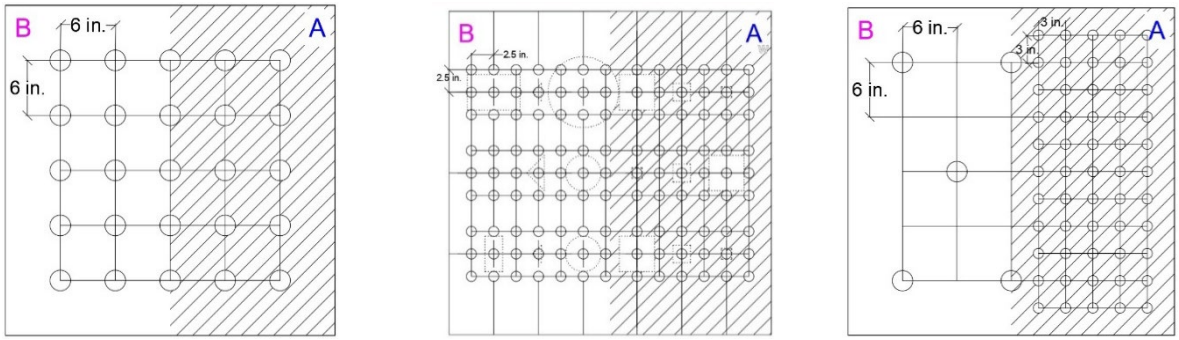

(a) Grid system for S1, S2, S4 (b) Grid system for S3 (c) Grid system for S5

Figure 13. IE data acquisition process

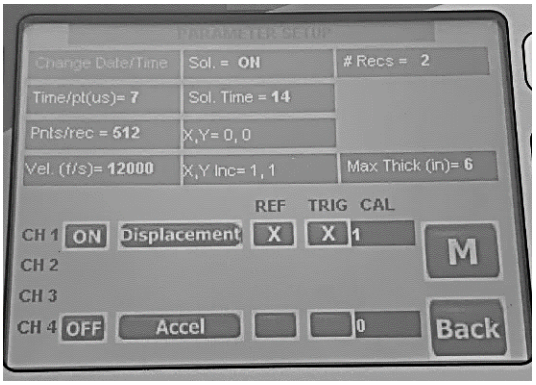

Figure 14. IE data acquisition parameters

The IE firmware for the NDE-360 includes a feature called ‘IE Thickness Vel Cal’ which calculates the concrete velocity (ft./s) of a specimen with known thickness (depth). This option allows the user to precisely calibrate the concrete velocity at any location for accurate echo depth estimation. Because the slab thicknesses were known and uniformly maintained for this study, concrete velocity calibration was performed for each slab next to all four edges and then averaged for extracting high-quality IE data. Table 4 shows the average concrete velocity for the four concrete slabs derived from the calibration. The control slab (Slab 4) exhibited the highest concrete velocity since no artificial defects were implanted. On the other hand, the slab with voids (Slab 3) produced the lowest velocity of concrete.

CHAPTER 4

RESULTS AND DISCUSSION

Identification of Structural Defects with GPR Data

In this study, three different types of GPR scans (A-scan, B-scan, and C-scan) were used to identify the structural defects embedded in concrete slabs. GPR data obtained after 28-days curing of concrete was considered for analysis as suggested by earlier studies (Daniels, 1996 and Oikonomopoulou et al., 2022). When using the GPR images, three key factors were considered for identifying the defects in the concrete specimen: (i) finding the visibility or shape of a defect, (ii) estimating the location or depth of a defect, and (iii) determining the size (length, width, thickness) of a defect. The control slab GPR images were used to establish a stable and unchanging baseline for the GPR data. To avoid the interpretation problems caused by time-zero reflections, GPR images from defective slabs were compared to images from control slab. Benedetto et al. proposed using a time-zero reference when using A-scans to measure the depth of inhomogeneity at various locations Benedetto et al., 2017).

Determining the Visibility or Shape of a Defect

Table 5 summarizes the GPR results for defect visibility and detection based on the three types of scans. For specimen S2, the 14-day scan results showed evidence of delamination from the two different types of Polystyrene sheets, as illustrated in figures 15 (b) and 16 (b). After the concrete had cured for 28-days, the shapes were clearly distinguishable as can be seen in figures 15(c) and 16(c). The same behavior was observed in specimen S5, where corroded rebars were employed to detect corrosion (figure 17). One possible explanation for this phenomenon is that the moisture content of concrete varies with age (Hedjazi and Kabir, 2022), which will be discussed in greater detail in section 5. Furthermore, GPR C-scan data confirmed the definitive shapes of three corroded rebars in specimen S5 as shown in figure 18(c). The C-scan data of S2 also produced credible shapes for the two Polystyrene sheets simulating delamination. However, GPR results for specimen S3 were ambiguous to picture any delamination targets embedded at

two different sides. Trace[1] was retrieved using A-scan data, but the results were anomalous when compared to the actual location or shape of the defect. Moreover, C-scan data was unable to portray the shape of any of the small objects (polystyrene blocks) simulating delamination (Janku et al., 2019). This could be due to the dense meshing of the delamination objects at a small depth (Sangoju and Ramanjaneyulu, 2015). According to Ahmed et al., spacing between metal targets embedded at the same depth must be greater than 2 in. (50 mm) in order to avoid the targets appearing as a single object and acting as an irregularly shaped metal sheet during GPR scans (Ahmed et al., 2020). Additionally, Coleman et al. used statistical analysis to prove that GPR cannot differentiate between shallow delamination in plain concrete as a result of the apparent random amplitude distribution in the sample (Coleman et al., 2022). As a result, closely spaced delamination targets are very likely to result in incorrect GPR images.

It is worth noting that GPR did not detect the honeycomb and voids (simulated by balloons) on or near the top surface of specimen S4. This could be due to the proximity of the defects to the surface or the inability of GPR to detect surface defects (Yehia et al., 2014). Furthermore, GPR images failed to provide adequate information on structural voids simulated by PVC pipes. This is inconsistent with prior studies (Prego et al., 2017). The detectability of an object is highly dependent on the difference in Dk values between two materials. As a result, the resulting reflection of PVC (Dk = 4.0) must be strong, as its Dk value is considerably lower than that of concrete (Dk = 6.6 at test date). Unfortunately, this is not the case due to signal interference. The PVC pipes shared a common plane for wave propagation since they were placed on the top of each other. This can result in signal attenuation as the Dk of the medium has not changed. Therefore, GPR was unable to detect voids because it relies on wave velocity to establish the depth of medium. Another factor could be the small inner diameter (1/4 in. or 0.64 cm) of the PVC pipes (Yehia et al., 2014).

On the other hand, B-scan and C-scan images showed proof of voids simulated by plastic bottles in specimen S4. Line scans (L6 and L9) taken perpendicular to the longitudinal axis of the plastic bottles discovered voids embedded in the center of the concrete slab. While voids close to the edge were difficult to distinguish. The situation is identical for images obtained from area scans (A1 and A2). There

were no traces of voids for scans taken parallel to axis of plastic bottles. This supports the findings of prior GPR studies on the detection of elongated targets (Jiao et al., 2020).

Table 5: Summary of GPR test results

Specimen ID	Embedded Defects				Identification Type	
	C	DL	H	V	Visibility	Shape
S2	-	√	-	-	Y	S
S3	-	√	-	-	Y	U
S4	-	-	×	-	N	U
	-	-	-	√	Y	U
S5	√	-	-	-	Y	S
Note:	Defect detected = √ Defect not detected = ×		Y = yes N = no		S = satisfactory U = unsatisfactory	

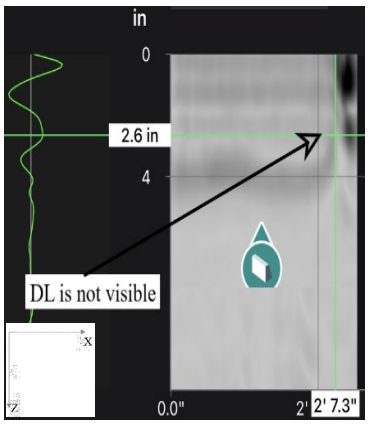

(a) 7-day

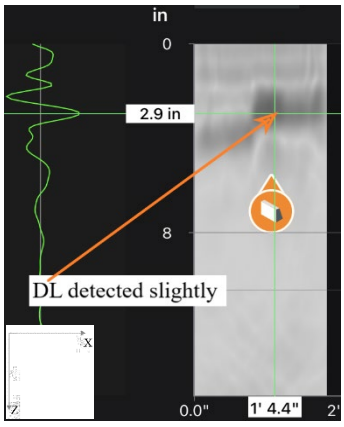

(b) 14-day

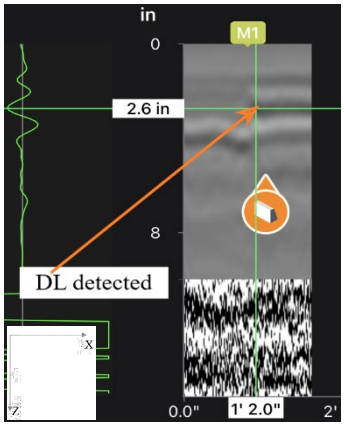

(c) 28-day

Figure 15: A-scan and B-scan data S2 (side A)

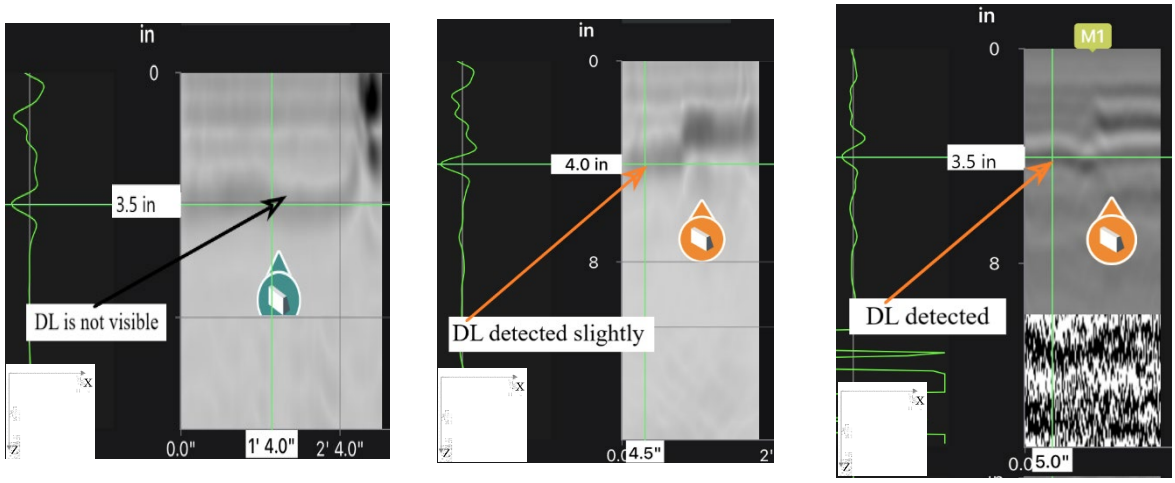

(a) 7-day (b) 14-day (c) 28-day

Figure 16: A-scan and B-scan data S2 (side B)

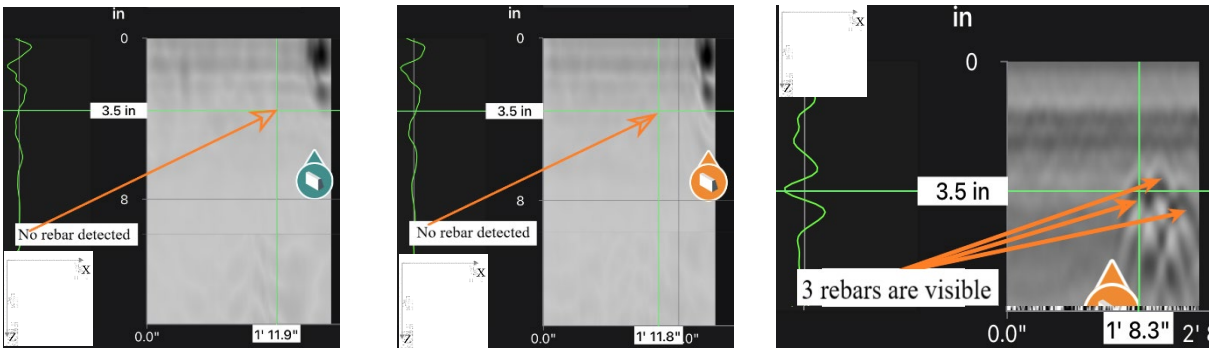

(a) 7-day (b) 14-day (c) 28-day

Figure 17: A-scan and B-scan data for S5 (side A)

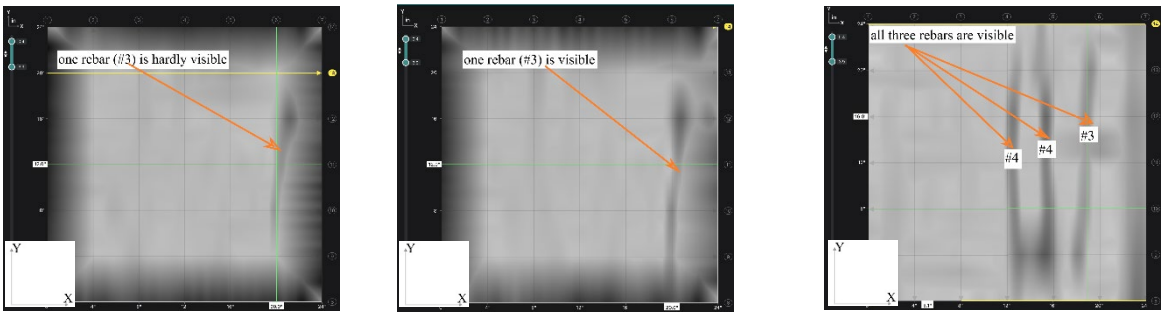

(a) 7-day (b) 14-day (c) 28-day

Figure 18: C-scan data for S5 (side A)

The following conclusions can be drawn about identifying the visibility and shape of the defects using GPR images from A-scan and B-scan:

a) *Corrosion:* A significant feature of the GPR data is the hyperbolic shape of the rebar in the B-scan radargrams as shown in figure 19(a). However, the scan direction and the rebar axis must be nearly perpendicular in order to obtain the hyperbolic shape. Otherwise, the shape will be asymmetric. If the scan direction is parallel to the rebar axis, GPR will register reflections from the top of the rebar rather than diffractions. Because B-scan images are typically a combination of reflections and diffractions, hyperbola fitting may result in incorrect rebar estimation (Forte and Pipan, 2017). A bright, narrow hyperbola indicates the presence of rebar embedded in well-cured concrete. Furthermore, narrow hyperbolas represent the fastest EM wave propagation in concrete. If the concrete has a low and decreasing water content, the hyperbolic shape will be more recognizable. In contrast, if the concrete has a lot of moisture, the hyperbola will be blurry and wider in shape. The slower speed of EM wave propagation in concrete causes this wider-shaped hyperbola (Hasan and Yazdani, 2014). Alternatively, according to Raju et al. (2018), A-scan data can be used to evaluate reinforcing bar corrosion. The authors proved that corroded rebars have the highest reflected amplitude, and that amplitude values increased proportionally to corrosion activity (Raju et al., 2018). So, the maximum amplitude value from A-scan and the hyperbolic apex of the rebar from B-scan radargrams can be used together to find corrosion. Rebar corrosion cannot be estimated in this study due to the inability to obtain amplitude values from the GP app.

b) *Delamination:* It can be detected on B-scan radargrams by identifying an irregular strip pattern representing a cavity (filled with air) at the interface of surrounding concrete as shown in figure 19 (b). This strip can have a relatively large dimension depending on the size of the delamination. In contrast, delamination from A-scan data can be identified by the difference in polarity between the reflection wave and the incident wave (Jiao et al., 2020). When the EM wave approaches the upper edge of delamination (point between concrete and filling air), it generates a reflection wave with the same

phase polarity as the incident wave. Since concrete (Dk = 6.6 at test date) has a higher Dk value than air (Dk = 1.0), the resultant amplitude is positive. Therefore, at the lower edge of delamination (point between air and surrounding concrete), the amplitude is negative. When the polarity of the reflection wave is opposite to that of the incident wave, delamination can be identified if the two waves produced similar amplitude values. Since amplitude values could not be obtained from the GP app, depth of delamination from A-scan was determined using 'the envelope' (Sensors, 2022).

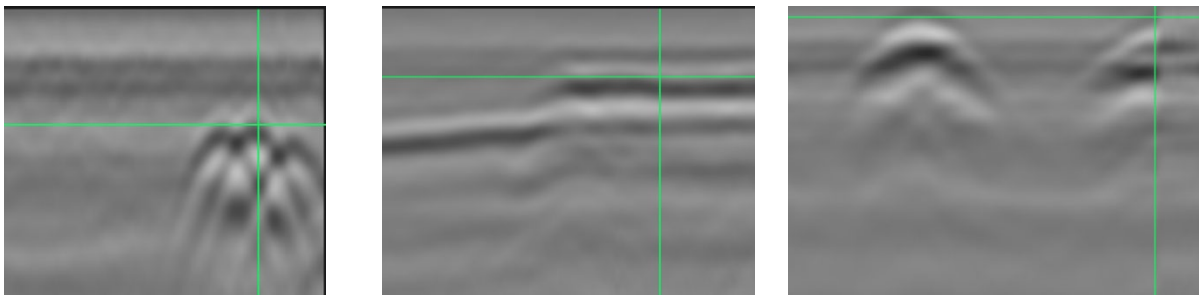

(a) Corrosion (b) Delamination (c) Voids

Figure 19: Pattern of defects from GPR B-scan data

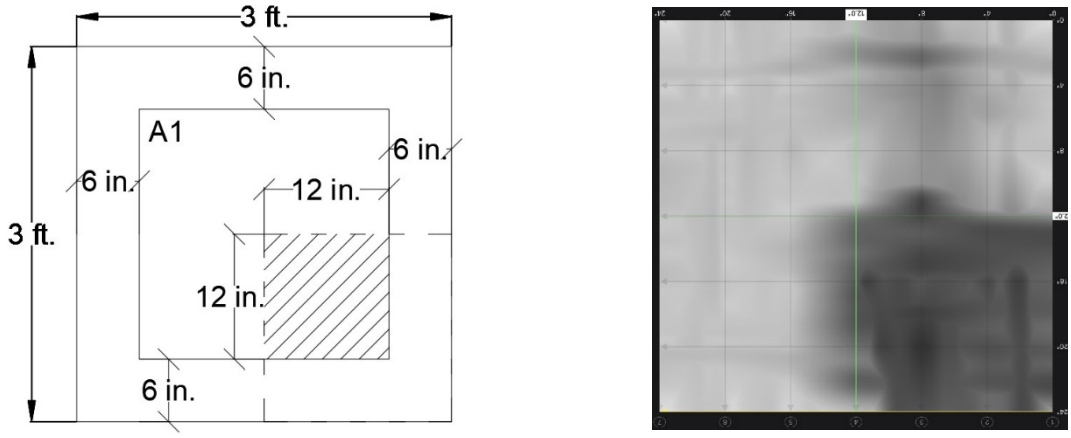

(a) (b)

Figure 20: Determining the size of delamination from C-scan data

c) *Voids:* B-scan radargrams showed a hyperbolic pattern for voids, similar to rebars. However, in this case, the hyperbola apex is either wide or flattened as shown in figure 19 (c). It is difficult to distinguish between hyperbolas obtained for rebars and voids due to the shape and reflectivity of the hyperbola. Jiao et al. proposed extracting a magnified view of the polarity change in radargrams to solve this problem (Jiao et al., 2020). In the case of voids, the transition between grey values changing from white to black and then back to white is more noticeable, as illustrated in figure 19 (c).

Table 6: Accuracy of GPR test results

Defect ID	Specimen ID (Side)	Line Scan ID	Actual Depth (in.)	Measured Depth (in.)		Absolute Deviation		Average Deviation		Absolute Error (AE)		Mean Absolute Error (MAE)		Mean Absolute Percentage Error (MAPE)		Mean Squared Error (MSE)	
				A-scan	B-scan	A-scan	B-scan	A-scan	B-scan	A-scan	B-scan	A-scan	B-scan	A-scan	B-scan	A-scan	B-scan
DL	S2 (A)	L2	2.5	2.6	2.5	0.05	0.05	0.15		0.10	0	0.20	0.10	20%	10%	0.04	0.01
		L3		2.8	2.3	0.25	0.25			0.30	0.20						
	S2 (B)	L2	3.5	3.7	3.6	0.05	0.05	0.08		0.20	0.10	0.20	0.25	20%	25%	0.04	0.06
		L3		3.7	3.9	0.10	0.10			0.2	0.4						
C	S5 (A)	L7	3.5	3.6	3.5	0.05	0.05	0.05		0.10	0	0.13	0.06	13.33%	6.77%	0.02	0.01
		L8		3.3	3.4	0.05	0.05			0.20	0.10						
		L9		3.4	3.6	0.10	0.10			0.10	0.10						

Determining the Location or Depth of a Defect

In order to assess the accuracy of GPR test results, the depth of structural defects discovered by GPR scans was compared to the as-built depth of the defects embedded in concrete slabs. The specimens S2 and S5 were chosen because the actual depth of the embedded defects (DL and C) can be verified for both (Table 1). As noted previously, the GP app did not provide amplitude values. As a result, using 'the envelope' obtained from A-scan, the depth of delamination and corroded rebars were calculated. Because the GP app computes measured depth from the top, the actual depth used here is a top-down estimate. For both defect types, the depth of Polystyrene sheets and rebars was determined using the bottom surface of B-scan radargrams. To determine the difference between measured and actual depth, statistical measures such as absolute deviation, average deviation, absolute error (AE), mean absolute error (MAE), mean absolute percentage error (MAPE), and mean squared error (MSE) were used, as shown in Table 6. The average deviation for corroded rebars depth was found to be 0.05, indicating that measured depths are closely distributed around the data set mean (n=2). This average deviation can be very useful in determining the thickness range of a defect. When using C-scans to collect GPR data, for example, delamination can be located within 2.35-3.575 inches, as shown later in section 4.3. The MAE values showed a significant deviation from the observed values for both A-scan and B-scan; however, GPR data was more accurate in both scans for detecting corroded rebars than delamination. The highest MAPE score for both A-scan and B-scan, on the other hand, was reported as 13.33% and 25% respectively. Given the range of 10% to 25%, this may be considered a reasonable margin of error for predicting depth of a defect (Swanson, 2015). Finally, MSE was calculated to account for atypical errors that were greater than the mean. The MSE values for all measurements were close to zero, with B-scan data having the highest MSE (0.06), demonstrating that all measured values were consistent with actual depth.

Determining the Size of a Defect

For specimen S2, GPR was able to determine the size of delamination simulated by two Polystyrene sheets embedded at different depths in concrete slab. In this case, the area scan (A1) obtained at the center of the

slab was taken into consideration. As shown in figure 20 (a), the standard 2 ft. × 2 ft. grid sheet was placed at the center of the slab. So, there was a 6 in. gap between each side of the sheet and the edge of the slab. Figure 20 (b) depicts the C-scan result, which shows a dark shade at a depth of 2.8-3.5 inches with a dimension of 12 in. 12 in. over a white background. This is understandable when viewed alongside the line scan data (as stated in section 4.2, the proposed range was 2.35-3.575 inches.). The overlapping of two delamination objects embedded at different depths produced somber shadows to represent the defected area. The depth range (2.8–3.5 inches) obtained from GP app is also comparable to the actual depth of the delamination. Since the smaller Polystyrene sheet (1.5 ft. × 1.5 ft.) was placed at the corner of specimen S2, the resulting GPR images show parallel findings for the embedded delamination size (length × width). On the other hand, B-scan radargrams can be used to determine the thickness of the two Polystyrene sheets. The line scan (L2 and L3) data used in Table 4 yielded an average thickness of 0.45 in. for both sides (A and B). Error rate was calculated using equation 2 as given below. The accuracy of delamination thickness detection is 80 percent according to equation 3, which is considered satisfactory. Additionally, the radius-to-depth ratio (R/d ratio), for the simulated defects was calculated. In equation 4, the smallest dimension is the average thickness (0.45 in.) obtained from B-scan data, and the average depth of defect is the average of measured depths for line scan (L2 or L3), as mentioned in Table 7. In both instances, R/d ratios were found to be 0.12 and 0.18, proving that GPR scans can successfully identify continuous delamination for thicknesses as low as 0.12 inches.

$$Error\ Rate = \frac{(Average\ Thickness - Actual\ Thickness)(in.)}{Actual\ Thickness\ (in.)} \times 100 \quad \text{(Equation 2)}$$

$$\text{Accuracy (\%)} = 100 - Error\ Rate \quad \text{(Equation 3)}$$

$$R/_d\ ratio = \frac{smallest\ dimension\ of\ the\ defect\ (in,)}{average\ depth\ of\ the\ defect\ (in.)} \quad \text{(Equation 4)}$$

Table 7: Validity of GPR test results

Defect ID	Specimen ID (Side)	Line Scan ID	Actual Thickness (in.)	Measured Thickness (in.)	Average Thickness (in.)	Accuracy (%)	Average Depth (in.) [avg. of Measured Depth from Table 4]	R/d ratio
DL	S2 (A)	L2	0.375	0.4	0.45	80	2.55	0.18
		L3		0.5				
	S2 (B)	L2	0.375	0.3	0.45	80	3.725	0.12
		L3		0.6				

Factors Affecting GPR Data

(i) Concrete age: Although data were collected at 7, 14, and 28 days upon concrete casting, simulated defects became apparent in all concrete slabs by the time of 28 days. For instance, DL was not visible at 7-day and 14-days scan results for S2 on both sides (A and B) as shown in figure 12. Moreover, as shown in figure 13, the GPR could only find one rebar until day 28. This is consistent with the findings of Yehia et al., who used a 0.45 water-to-binder ratio for lightweight concrete (Yehia et al., 2014). Because of the porous aggregate microstructure, it is difficult to obtain clear GPR images from fresh concrete.

(ii) Dielectric constant: Furthermore, the Dk was found to decrease slightly with concrete age as shown in Table 2. As concrete ages and absorbs free water, Lai et al. proposed that this change will diminish once it reaches a tipping point (at about 60 days) (Lai et al., 2009). The GP8000 showed the same Dk for all concrete slabs after obtaining the calibration for one slab. Although data for each concrete slab were collected on different days, the variation in Dk remained insignificant.

(iii) Environmental factors: To minimize the effect of moisture loss due to drying, the GPR scans presented here for analysis were collected on the same day (Agred et al., 2018). Table 2 shows the environmental

factors such as relative humidity and average temperature recorded for all events at the time of data collection (12pm to 5pm). According to the findings, environmental factors had no effect on the GPR (GP 8000) used in this study to calibrate Dk and identify structural defects in concrete slabs. This is consistent with previous research findings (Yehia et al., 2014). Other studies have found that moisture can greatly impact GPR signals, reducing the penetrating ability of EM waves and thus resulting in inaccurate images of embedded concrete defects. This impact is more apparent in freshly hydrated concrete and in concrete that is constantly exposed to high temperatures and humidity. As a result, it is critical to confirm that an equilibrium has been attained before collecting GPR data from the experimental investigation. For newly constructed concrete ground slabs, 3 months is often thought to be adequate to establish the equilibrium. This period may be shorter for specimens in direct contact with air. It has been proposed that moisture content and dielectric constant reach their limiting values after 6 months (Oikonomopoulou et al., 2022).

(iv) Overlapping of defects: Defects in concrete slabs, when distributed on top of each other (specimen S4), cause signal interference. This is due to the fact that both the incident and reflected signals travel along the same plane. Therefore, the signal wave may be attenuated, leading to erroneous or missing reflections for the embedded defects.

(v) Noise from slab edge/surface: GPR images for all specimens, including the control specimen, demonstrated a dark shade for the top 0.9 in (B-scan) and a comparable shade around the slab edges (C-scan). This might occur because of the air gap between the device and the concrete surface. Previous research has indicated that if scans can be taken over a sand bed, unnecessary waveforms from backfill noise can be avoided (Lai et al., 2018).

Identification of Structural Defects with IE Data

IE tests were carried out on the concrete slabs using the concrete velocity obtained from calibration for each slab (Table 3). To collect the IE data, an impulse is applied by the integrated solenoid impactor of the IE test head as it is pressed against a single point on the surface of the concrete slab. Data were recorded from each test point in accordance with the pre-determined testing grid that was laid out on

the surface of the concrete slabs. The forcing function caused the impactor solenoid to produce broad and constant spectral waves on the test point or element. The displacement sensor (transducer) attached to the IE head measures the corresponding displacement at each test point generated by the spectral waves. For natural frequencies, the significant maxima (peaks) for the resonant spectral waves were obtained using FFT. As a result, the transducer converts the measured displacement into an analog signal of amplitude vs. time, called 'waveform'. The waveform is recorded by the data logging system (WinIE software), which is then processed for data analysis in either the time-domain or frequency-domain. For normal mode data with thicknesses less than 6 inches (15cm), a higher frequency high-pass filtering is recommended for data analysis (Kee et al., 2012 and Test, 2008). All IE signals considered for analysis were subjected to the default scale. Based on the current filter (high pass) settings, the WinIE software automatically detects the dominant frequency peak of the spectrum and calculates the subsequent echo depth.

Time-domain analysis for damage detection

In this study, the characteristics of IE signals extracted from the time-domain analysis were used to identify the embedded defects in concrete slabs. The features of the IE signals in the witness (or control) slab were compared to those of the defective concrete slabs for this purpose. Figures 21–25 show the typical time-domain response from the IE tests on the concrete slabs. The characteristics of IE signals for control slab support the findings of previous research, indicating that the amplitude (voltage) of IE signals collected from sound concrete (no defect) is generally more concentrated in short intervals when compared to defective concrete (Jafari and Dorafshan, 2021). Figures 22 (b) and 24 (a), on the other hand, show IE signal data demonstrating concentrated signal length for concrete slab with artificial defects. As a result, time-domain analysis of IE data cannot distinguish between sound and damaged concrete with precision. Furthermore, it is difficult to find the optimal IE signal for a specific defect type; thus, they cannot be used to classify the defect type in concrete.

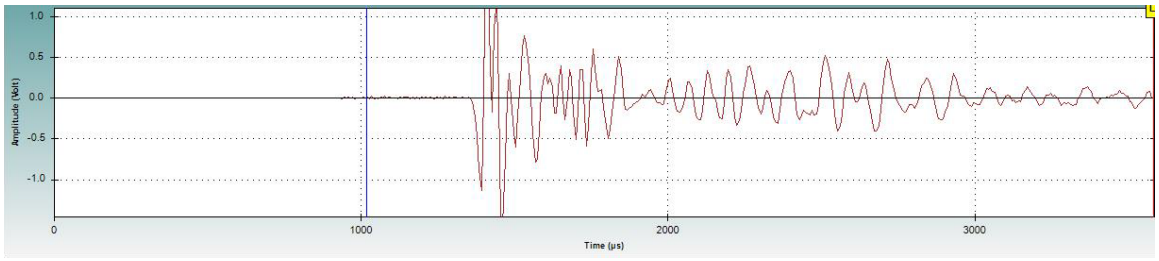

(a) At the edge of the slab

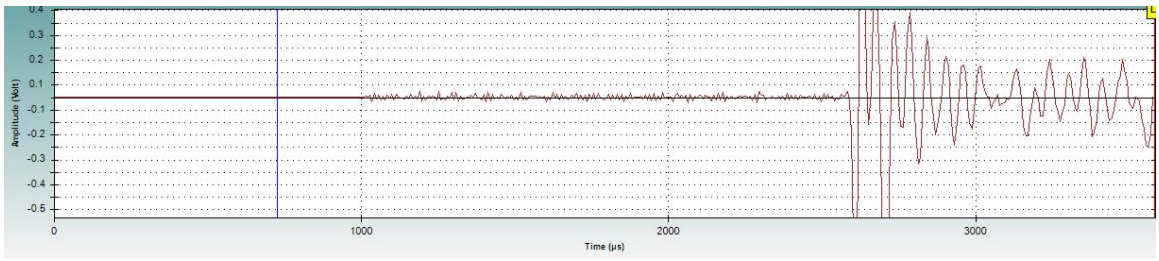

(b) At the center of the slab

Figure 21: Typical time-domain signal for slab with no defects (specimen S1)

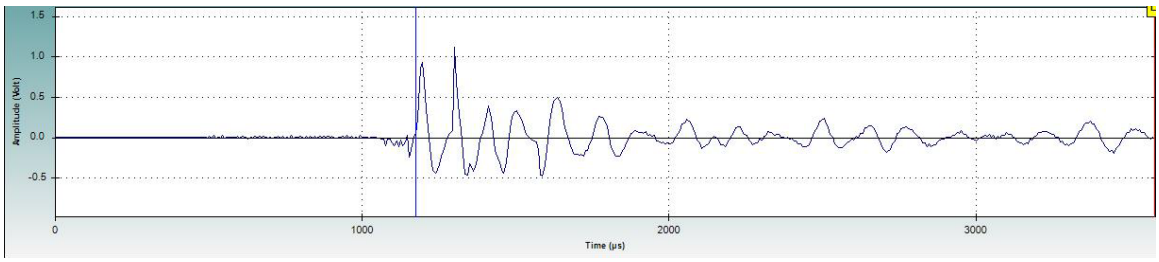

(a) At two layers (side A)

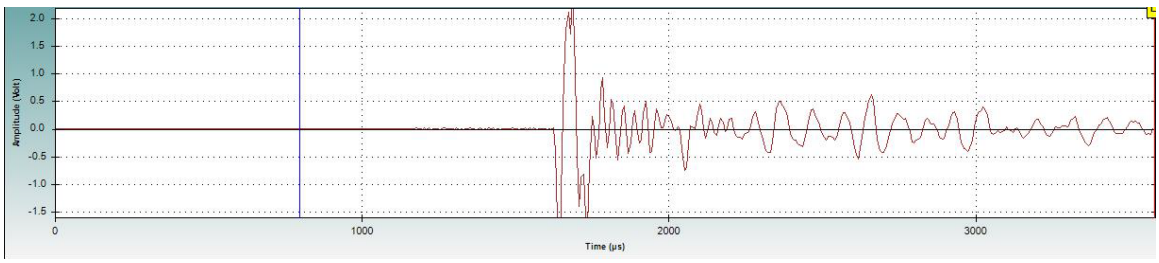

(b) At one layer (side B)

Figure 22: Typical time-domain signal for slab simulating delamination (specimen S2)

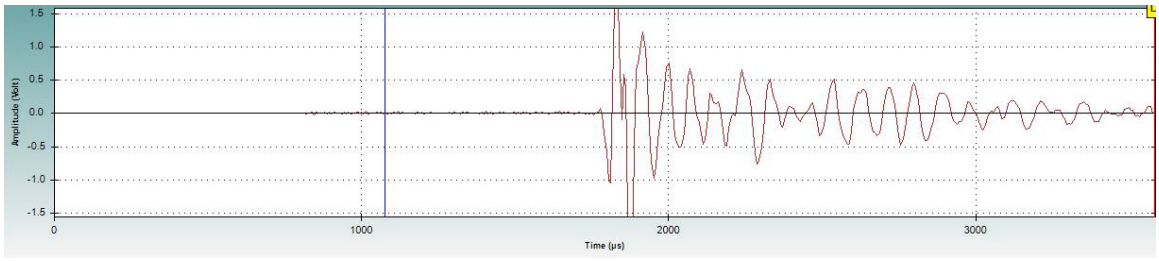

(a) At side A

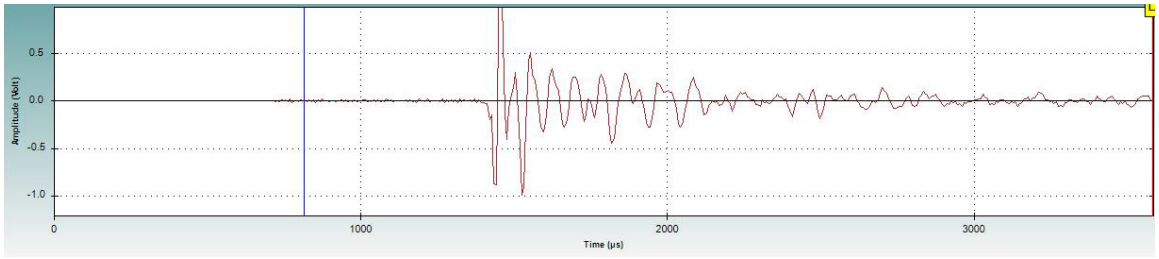

(b) At side B

Figure 23: Typical time-domain signal for slab simulating delamination targets (specimen S3)

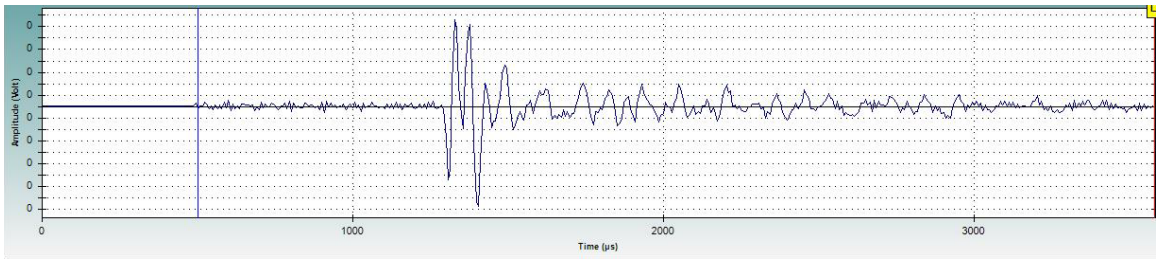

(a) By plastic bottles (side A)

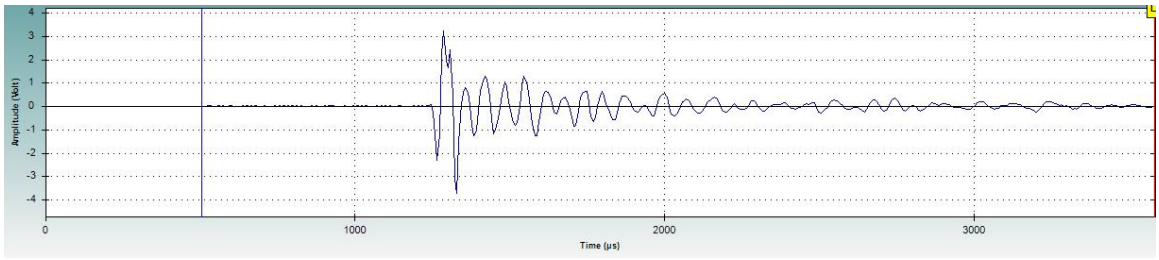

(b) By PVC pipes (side B)

Figure 24: Typical time-domain signal for slab simulating voids (specimen S4)

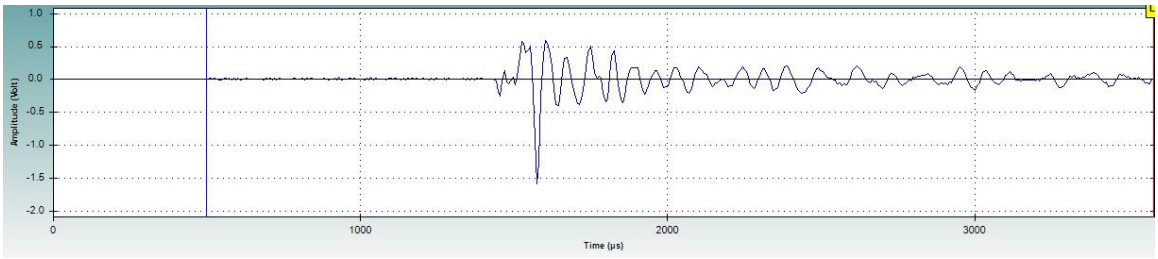

(a) Defect zone with corroded rebars (side A)

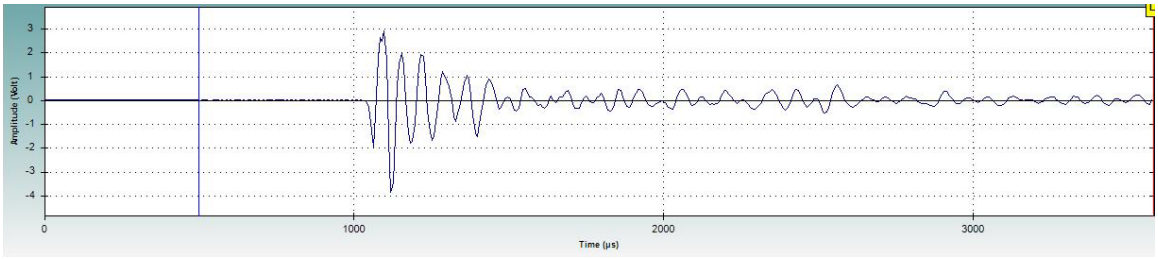

(b) Sound zone with no defects (side B)

Figure 25: Typical time-domain signal for slab simulating corrosion (specimen S5)

Previous research indicates that IE signals from sound concrete can produce one distinct peak point within its length, whereas IE signals from defected concrete can produce two or more distinct peaks within its period (Sengupta et al., 2021). However, in this study, IE signals from the control slab (no defect) showed two major peaks both at the center (Fig. 21a) and at the edge (Fig. 21b). Additionally, the sound zone (no defect) of specimen S5 showed multiple IE signal peaks in shorter time (Fig 25b). The concrete slab with delamination targets, however, showed a single, distinct peak as shown in figure 23 (b). IE data from either flawed or normal concrete did not follow any discernible trend. As a result, time-domain analysis of IE signals cannot be used to detect damage in concrete slabs.

Frequency-domain analysis for damage detection

The purpose of frequency-domain analysis of IE data is to determine the dominant frequencies in the recorded waveform. An amplitude spectrum, which displays the amplitudes of the various frequencies present in the waveform, is produced by the FFT. The thickness frequency is usually the dominant peak in the spectrum of plate-like structures. Using equation 1, the value of the peak frequency

in the amplitude spectrum can be used to calculate the depth of the reflecting interface (defect depth). Table 8 summarizes the IE test results for the calculated depth (from the peak frequency) and actual depth of the embedded defects. A single, distinct peak was seen in the IE spectrum data for concrete slabs with no defects (Figs. 26a, 26b, and 30b). The resulting depth for both specimens S1 and S5 was approximately 4.9 inches, which is close to the specimens' actual thicknesses (S1 = 5 in. and S5 = 5.5 in.). This corresponds to the interpretation of IE data from bridge inspection for a sound deck (in good condition) (Test, 2008).

Table 8. IE test data from frequency spectrum

Specimen ID		Defect Type	Actual Depth (in.)	Calculated Depth from IE (in.)	Peak Frequency (Hz.)
S1		Control slab	5.0	4.9	17299
				4.8	17578
S2	Side A	Delamination	2.5	4.7	12834
	Side B		3.5	6.1	10044
S3	Side A	Delamination targets	2.5	4.4 – 7.2	7812 – 12834
	Side B		3.5	6.1 – 8.4	6696 – 9207
S4	Side A	Voids (bottle)	0 – 2.5	2.5	19252
	Side B	Voids (PVC pipe)	2.5 – 3.5	3.0	15904
S5	Side A	Corrosion	3.5	7.2	9765
	Side B	Control slab	5.5	4.9	14229

According to Gucunski et al. delamination in a concrete slab can be identified by a downshift in the frequency peak, which results in an increase in apparent thickness and is in good agreement with IE spectrum results for the concrete slabs simulating delamination (Gucunski et al., 2008). When compared to control slab test values, the apparent thickness of specimen S2 reached to 6.1 inches, while the

peak frequency dropped from 17 kHz to 10 kHz (Fig. 11). Since the peak frequency for the delaminated slab is lower than the peak frequency for the control slab, the resulting delamination depth exceeds the slab thickness according to equation 1. This is because the dominant response of large, delaminated areas in concrete slabs is characterized by flexural mode oscillations of the delaminated portion of the concrete rather than the slab bottom (Abdelkhalek and Zayed, 2020). However, IE results could not determine the actual depth of delamination. This could be because the lateral dimensions of the delamination were greater than 1.5 times its depth. As a result, the defect behaves as an infinite boundary, with the response of a plate of thickness equal to the flaw depth (Yehia et al., 2014). The IE transducer did not detect delamination targets smaller than 4 inches (specimen S3). This is because the lateral dimensions of the delamination targets were less than one-third of their depth (Sansalone and Streett, 1997).

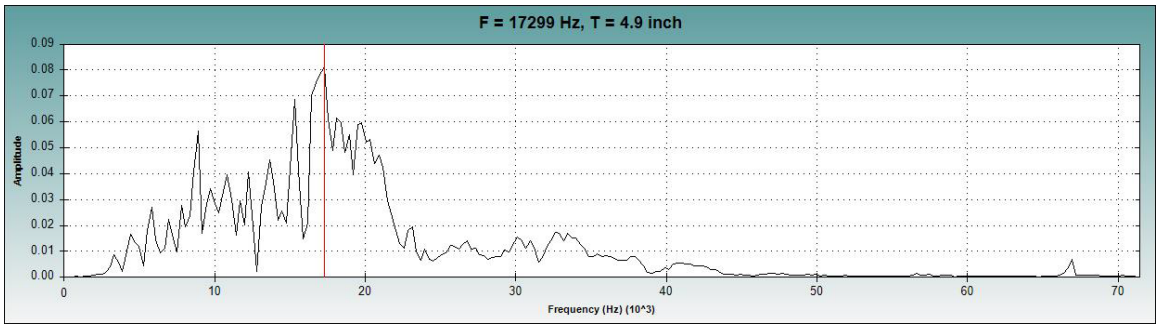

(a) At the edge of the slab

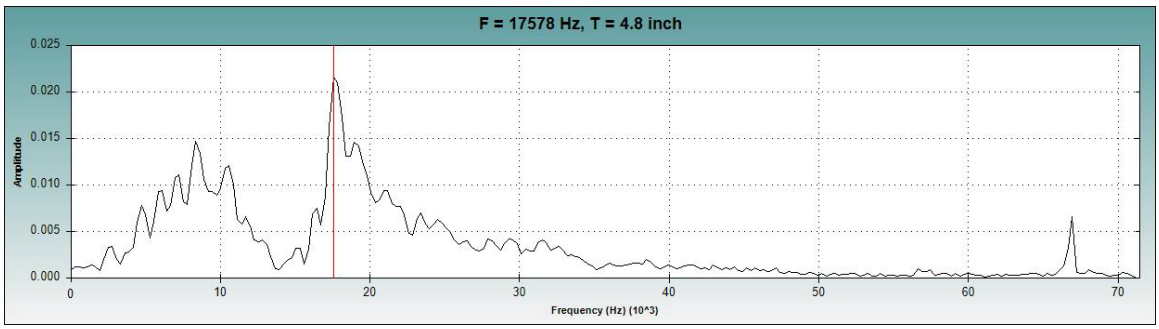

(b) At the center of the slab

Figure 26: Typical frequency spectrum for slab with no defects (specimen S1)

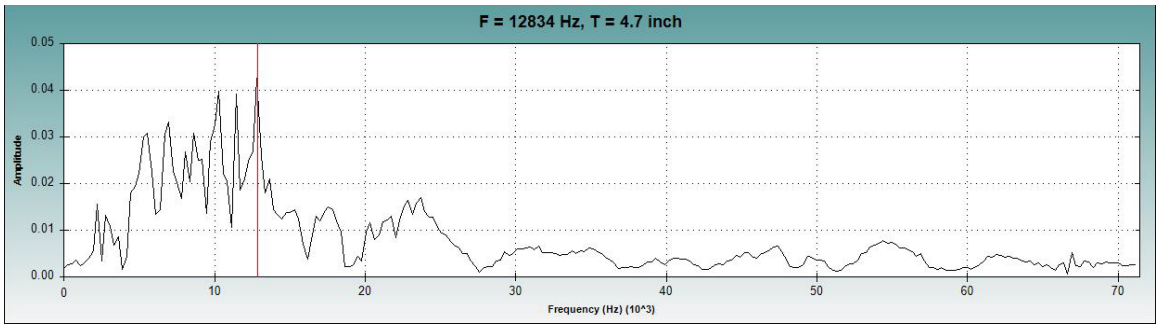

(a) At two layers (side A)

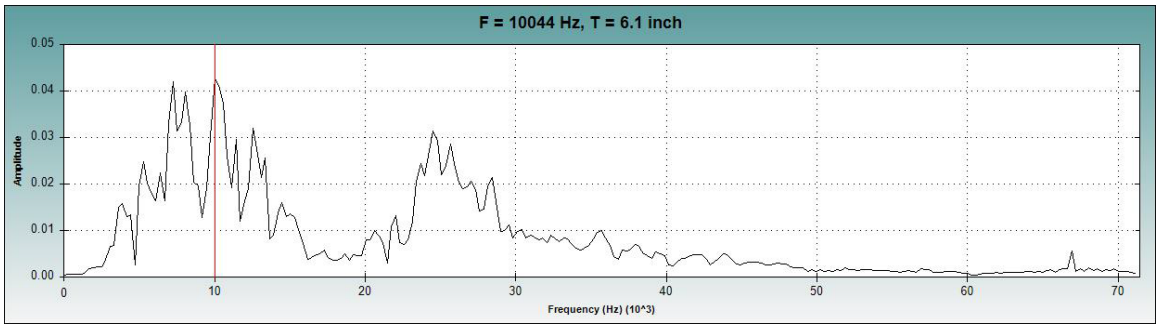

(b) At one layer (side B)

Figure 27: Typical frequency spectrum for slab simulating delamination (specimen S2)

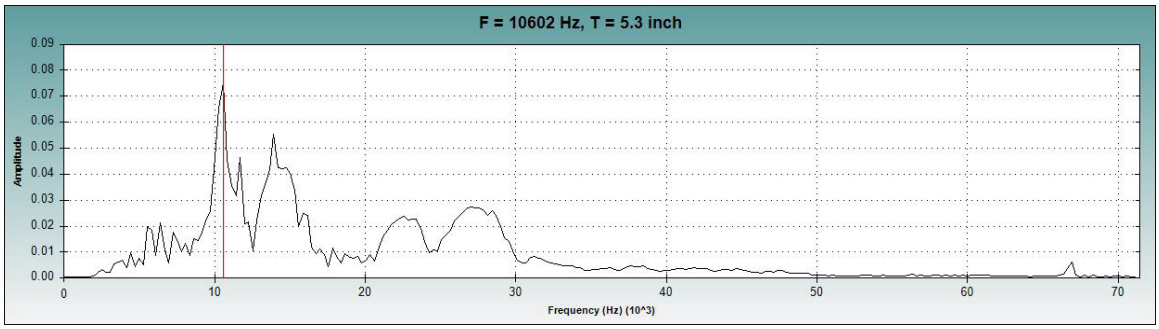

(a) At side A

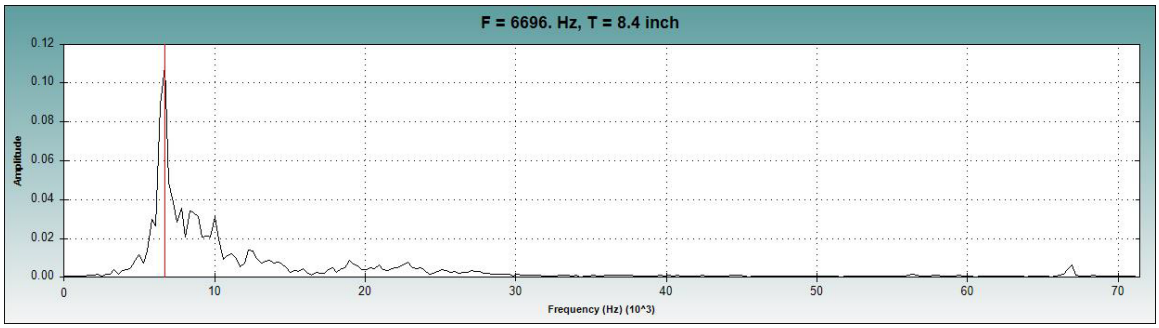

(b) At side B

Figure 28: Typical frequency spectrum for slab simulating delamination targets (specimen S3)

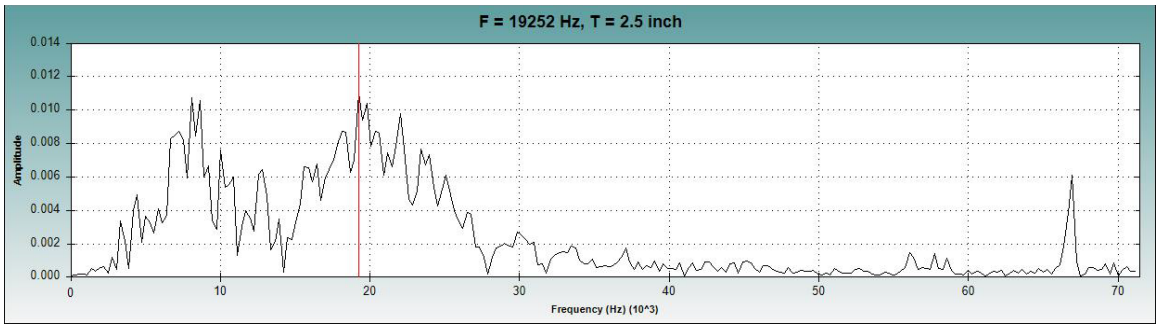

(a) By plastic bottles (side A)

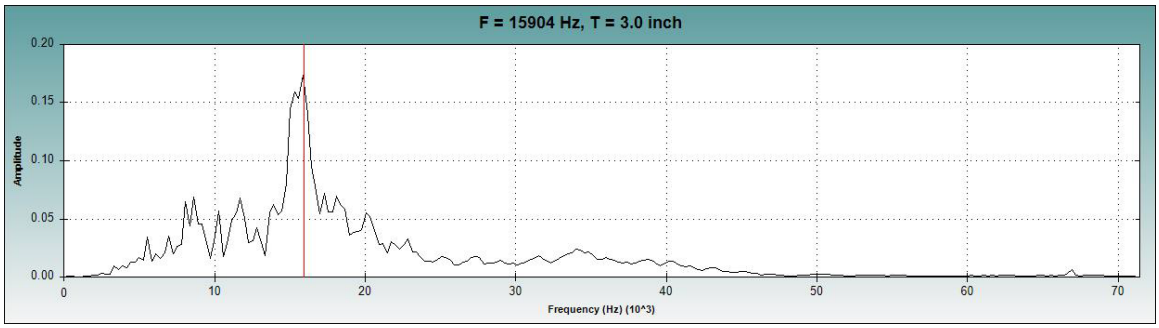

(b) By PVC pipes (side B)

Figure 29: Typical frequency spectrum for slab simulating voids (specimen S4)

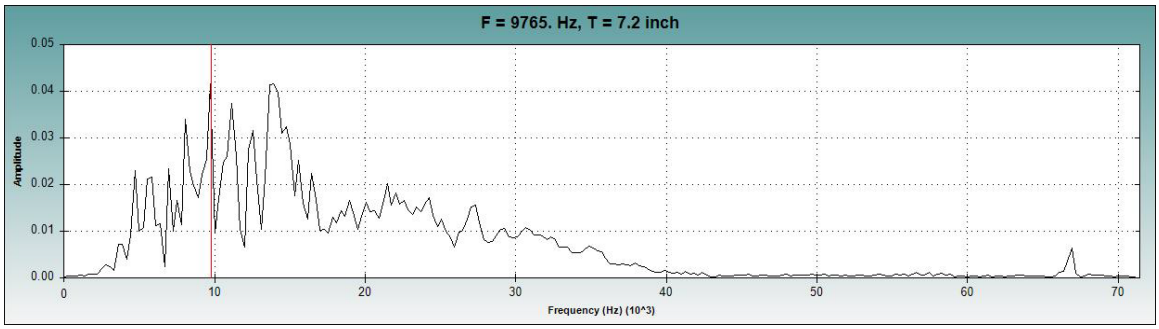

(a) Defect zone with corroded rebars (side A)

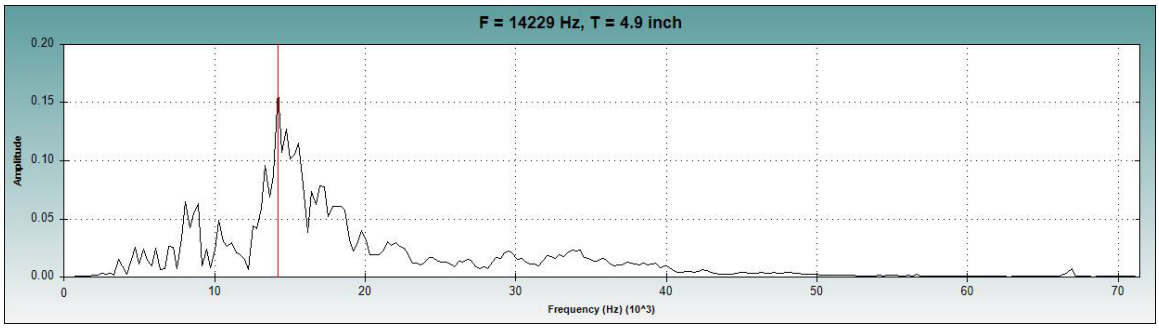

(b) Sound zone with no defects (side B)

Figure 30: Typical frequency spectrum for slab simulating corrosion (specimen S5)

The IE spectrum data characterized the voids simulated by plastic bottles with two distinguished peaks (maximum frequency = 19252 Hz.) and a single peak for PVC pipes (maximum frequency = 15904 Hz.), as shown in figures 29 (a) and 29 (b). Because of the higher peak frequency in comparison to the control slab, the resultant depths for specimen S4 were 2.5 inches and 3.0 inches for the IE head placed above voids simulated by bottles and pipes, respectively. These values are less than the actual thickness of the slab (S4 = 5 in.). This is because of the fact that little to no energy is being propagated towards the bottom of the slab (Abdelkhalek and Zayed, 2020). Due to the close overlapping of PVC pipes at two layers, all voids simulated by PVC pipes were not detected (Carino, 2001). Corroded rebars from specimen S5 produced higher thickness value (7.2 inches) and multiple frequency peaks (maximum frequency = 9765 Hz.), as shown in figure 30 (a). In all of the defected concrete slabs, defects embedded at the 2.5-inch layer (side A) resulted in lower calculated thicknesses and higher peak frequencies for all tested points when compared to defects embedded at the 3.5-inch layer (side B). This is in good agreement with previous research findings (Abraham et al., 2000 and Sansalone & Streett, 1997). If the contact time for the impactor is too long, the amplitude spectrum will lack a peak corresponding to the flaw depth. Previous research found that if the contact time is less than three-quarters of the P-wave travel time, the depth of a sufficiently sized planar flaw could always be measured (Pospisil et al., 2021). However, because the solenoid impactor is integrated with the IE head and automatically applies the impulse in the concrete surface, the IE used in this study could not precisely address the defect depth.

Comparison of damage detection capabilities between GPR and IE

In order to validate the damage detection results of this study, the IE frequency-domain data for the concrete slabs were compared to the GPR test results on the same concrete specimens. Table 9 summarizes the findings from the two NDT methods (GPR, and IE) for detecting structural damages in concrete slabs. For concrete slabs with no defects, IE tests were more reliable than GPR because the IE results not only estimate the thickness of the slab precisely but also illustrate a unique frequency spectrum shape to distinguish between sound and defective concrete (Fig. 26). GPR, on the other hand, outperformed

IE in identifying large delamination areas or objects embedded in two different layers of a concrete slab. While the two delamination layers were clearly visible in the GPR line scan data for specimen S2 (Fig. 16), identifying the defect in the IE scans (Fig. 27) was more difficult because additional thickness and frequency data analysis is required. Furthermore, GPR line scans identified the depth (location) of the defect, and GPR area scans successfully determined the size of the delamination. IE, in contrast, detected delamination, but precise measurement of the defect is still not fully automated. When it came to locating small delamination targets, IE data proved to be more dependable than GPR. When compared to the actual location or shape of the small delamination targets, the GPR results were anomalous. Due to signal attenuation caused by overlapping of PVC pipes in two layers, GPR scans failed to detect voids on concrete. IE scans, on the other hand, detected voids near the top surface but were unable to identify voids placed at the following layer. Voids simulated by plastic bottles were easily obtained from IE frequency-domain data. GPR indicated a flat (or wide) hyperbolic shape for voids in line scan data but was unable to determine detailed measurements from area scans. GPR was more effective and precise than IE at locating corroded rebars for the experimental concrete specimens, which is consistent with previous research (Pospisil et al., 2021). The comparison of scan data from shows that GPR is more accurate in detecting damages simulated by metallic objects, whereas IE can detect damages regardless of the type of simulated object.

Table 9. Comparison of test results between IE and GPR

Defect Description	Defect Depth (in.)		Defect Thickness (in.)	
	IE	GPR	IE	GPR
Large delamination at one layer	4.7	2.3	-	0.3
Large delamination at two layers	6.1	3.6	-	0.4
Small delamination targets	4.4	2.9	-	-
Voids simulated by plastic bottles	2.5	1.8	-	-
Voids simulated by PVC pipes	3.0	1.8	-	-
Corroded rebars	4.9	3.4	-	-

CHAPTER 5
CONCLUSIONS AND RECOMMENDATIONS

Conclusions

This study investigated the potential of two NDT methods such as, GPR and IE, to determine the shape, size, and depth of simulated concrete defects. GPR images obtained with automatic gain adjustment and noise cancellation from the equipment were used to identify structural defects embedded in concrete slabs. The results suggested that GPR data cannot be used for identifying structural defects in freshly poured concrete slabs due to the high moisture content of concrete at early ages. Therefore, concrete specimens must be cured for at least 28 days before undertaking GPR scans. According to B-scan data, the simulated defects followed a consistent pattern; hyperbolas for voids and corroded rebars, and rectangular strips for delamination. The area scan data for specimen S2 showed a lower R/d ratio of 0.12 and an accuracy of 80 percent for determining the thickness of delamination. The statistical results showed an average deviation of 0.15 (n = 2) for the measured depth of delamination from GPR data. But GPR did not detect delamination simulated by objects measuring 8 inches or less in length or width, or objects that were placed 2 inches apart. This study suggests that dense scan spacing (5 scans/inch) can detect structural defects embedded in concrete slabs at a shallower depth (2.5 inches). However, when embedded defects share a common plane, signal interference can lead to inaccurate or misleading GPR data. On the other hand, IE testing used a grid system of transverse and lateral gridlines marked on the top surface of the specimens to cover the entire defect or defect areas in order to identify embedded defects. When compared to the control slab, concrete slabs with simulated defects had IE time-domain signals distributed over long-time intervals. There was no ideal IE signal for a specific defect type, nor was there any discernible pattern in peaks for IE signals from time-domain data that could be reported from the investigation. As a result, IE time-domain data is unlikely to be used to locate defects in concrete slabs, which is consistent with previous research. Simulated defects in concrete specimens were successfully localized using IE frequency-domain analysis. The two types of delamination simulated in this study resulted in a decrease in peak frequency values (from 17 kHz. to 10 kHz.) for concrete slabs when compared

to slabs without defects. Concrete slabs embedded with voids created by plastic bottles yielded the opposite results (peak frequency increased to 19 kHz.). However, IE results were unable to determine the precise depth of embedded defects. This is because the lateral dimensions of the delamination were greater than 1.5 times its depth. To validate the data, the IE frequency-domain results were compared to GPR data from another study involving the same specimens. The comparison of scan data from both studies demonstrated that IE could detect damages regardless of the type of simulated objects. However, GPR can provide a quantitative estimate of defect depth and size.

Limitations of the study

i. Although corroded rebars were identified in this study using GPR, actual corrosion could not be estimated because the GP app does not provide amplitude values.
ii. The use of corroded and uncorroded rebars in the same specimen could have provided a more accurate estimate of the reflection amplitude for simulated corrosion.
iii. Because the impactor used in this study for IE testing was integrated with the IE head, the contact time could not be precisely controlled to estimate a defect depth.

Implications for future research

i. Although automatic gain settings and noise cancellation were useful for collecting GPR data on the test specimen, they are not always the best way to identify defects.
ii. On the other hand, high-pass filtering was used during the analysis of IE data. This is recommended for cutting-off low frequency energy from the transducer. However, low-pass filtering is necessary for removing high frequency noise energy close to the test head.
iii. It is recommended to conduct research that includes manual adjustment for gain and noise sources for GPR, as well as using bandpass filtering to set upper and lower cutoffs for IE frequency data analysis.

REFERENCES

Abdelkhalek, S., & Zayed, T. (2020). Comprehensive inspection system for concrete bridge deck application: Current situation and future needs. Journal of Performance of Constructed Facilities, 34(5), 03120001.

Abouhamad, M.; Dawood, T.; Jabri, A.; Alsharqawi, M.; Zayed, T. (2017). Corrosiveness mapping of bridge decks using image-based analysis of GPR data. Automation in Construction. 80. 104-117. https://doi.org/10.1016/j.autcon.2017.03.004.

Abraham, O., Leonard, C., Cote, P., & Piwakowski, B. (2000). Time frequency analysis of impact-echo signals: numerical modeling and experimental validation. Materials Journal, 97(6), 645-657.

Agred, K., Klysz, G., & Balayssac, J. P. (2018). Location of reinforcement and moisture assessment in reinforced concrete with a double receiver GPR antenna. Construction and Building Materials, 188, 1119-1127.

Ahmad, A., & Bond, L. J. (2018). ASM Handbook: Nondestructive Evaluation of Materials (17). https://doi.org/10.31399/asm.hb.v17.9781627081900

Ahmed, S. B., El Qassas, R. A., & El Salam, H. F. A. (2020). Mapping the possible buried archaeological targets using magnetic and ground penetrating radar data, Fayoum, Egypt. The Egyptian Journal of Remote Sensing and Space Science, 23(3), 321-332.

Aktan, H. M., Fu, G., Dekelbab, W., & Attanayaka, U. (2003). Investigate causes & develop methods to minimize early-age deck cracking on Michigan bridge decks (No. Research Report RC-1437).

American Society for Testing and Materials. (2004). Test method for measuring the P-wave speed and the thickness of concrete plates using the Impact-Echo method. ASTM C1383 – 04. ASTM International, West Conshohocken, PA.

American Society for Testing and Materials. (2007). Committee D04 on Road and Paving Materials. Standard test method for detecting delaminations in bridge decks using infrared thermography. ASTM International, West Conshohocken, PA.

American Society for Testing and Materials. (2008). Standard test method for evaluating asphalt-covered concrete bridge decks using ground penetrating radar. ASTM D6087-08. ASTM International, West Conshohocken, PA.

American Society for Testing and Materials. (2011). Standard guide for using the surface ground penetrating radar method for subsurface investigation. ASTM International, West Conshohocken, PA.

American Society for Testing and Materials. (2019). Standard guide for using the surface ground penetrating radar method for subsurface investigation. ASTM D6432 – 19. ASTM International, West Conshohocken, PA.

American Society for Testing and Materials. (2022). Standard Test Method for Measuring the P-Wave Speed and the Thickness of Concrete Plates Using the Impact-Echo Method. ASTM C1383 – 15. ASTM International, West Conshohocken, PA.

Aseem, A., Baloch, W. L., Khushnood, R. A., & Mushtaq, A. (2019). Structural health assessment of fire damaged building using non-destructive testing and micro-graphical forensic analysis: a case study. Case Studies in Construction Materials, 11, e00258.

Benedetto, A. (2013). A three-dimensional approach for tracking cracks in bridges using GPR. Journal of Applied Geophysics, 97, 37-44.

Benedetto, F. and Tosti, F. (2017). A signal processing methodology for assessing the performance of ASTM standard test methods for GPR systems. Signal Processing. 132, 327-337. https://doi.org/10.1016/j.sigpro.2016.06.030.

Benedetto, A., Tosti, F., Ciampoli, L. B., & D'amico, F. (2017). An overview of ground-penetrating radar signal processing techniques for road inspections. Signal processing, 132, 201-209.

Caputo, F., Navarro, C., & de Castro, P. M. (2017). Failure Mechanisms and Damage Modelling for Advanced Materials. Advances in Materials Science and Engineering, 2017.

Carino, N. J. (2001). The impact-echo method: an overview. Structures 2001: A Structural Engineering Odyssey, 1-18.

Chaudhary, M. T. A. (2013). Effectiveness of Impact Echo testing in detecting flaws in prestressed concrete slabs. Construction and Building Materials, 47, 753-759.

Chen, F., & Qiao, P. (2015). Probabilistic damage modeling and service-life prediction of concrete under freeze–thaw action. Materials and Structures, 48(8), 2697-2711.

Clem, D. J., Popovics, J. S., Schumacher, T., Oh, T., Ham, S., & Wu, D. (2013, January). Understanding the impulse response method applied to concrete bridge decks. In AIP Conference Proceedings (Vol. 1511, No. 1, pp. 1333-1340). American Institute of Physics.

Coleman, Z. W., & Schindler, A. K. (2022). Investigation of Ground-Penetrating Radar, Impact Echo, and Infrared Thermography Methods to Detect Defects in Concrete Bridge Decks. Transportation Research Record, 03611981221101027.

Cotic, P., Kolaric, D., Bosiljkov, V. B., Bosiljkov, V., & Jaglicic, Z. (2015). Determination of the applicability and limits of void and delamination detection in concrete structures using infrared thermography. Ndt & E International, 74, 87-93.

Daniels, D. J. (1996). Surface-penetrating radar. Electronics & Communication Engineering Journal, 8(4), 165-182.

Dawood, N., Marzouk, H., Hussein, A., & Gillis, N. (2013). Nondestructive assessment of a jetty bridge structure using Impact-Echo and Shear-Wave techniques. Journal of Bridge Engineering, 18(8), 801-809.

Dinh, K., & Gucunski, N. (2021). Factors affecting the detectability of concrete delamination in GPR images. Construction and building materials, 274, 121837.

Drobiec, Ł., Jasiński, R., & Piekarczyk, A. (2010). Diagnostics of reinforced concrete structures, Methodology, field tests, laboratory tests of concrete and steel.

Drobiec, Ł., Jasinski, R., & Mazur, W. (2019). Accuracy of eddy-current and radar methods used in reinforcement detection. Materials, 12(7), 1168.

Ekenel, M., & Myers, J. J. (2004, August). Nondestructive testing of Dallas County bridge in Missouri, USA. In 16th World Conference on Nondestructive Testing, Montreal, Canada.

Forte, E., & Pipan, M. (2017). Review of multi-offset GPR applications: Data acquisition, processing and analysis. Signal processing, 132, 210-220.

Gibson, A., & Popovics, J. S. (2005). Lamb wave basis for impact-echo method analysis. Journal of Engineering mechanics, 131(4), 438-443.

Gucunski, N., Slabaugh, G., Wang, Z., Fang, T., & Maher, A. (2008). Impact echo data from bridge deck testing: Visualization and interpretation. Transportation research record, 2050(1), 111-121.

Hasan, A. E. (2012, May). The use of ground penetrating radar with a frequency 1 GHz to detect water leaks from pipelines. In Proceedings of the 16th International Water Technology Conference (IWTC16), Istanbul, Turkey (Vol. 710, p. 16).

Hasan, M. I., & Yazdani, N. (2014). Ground penetrating radar utilization in exploring inadequate concrete covers in a new bridge deck. Case Studies in Construction Materials, 1, 104-114.

Hedjazi, S., & Kabir, E. (2022). Effects of Cement Type, Water-Cement Ratio, Specimen Size, and Curing Time on Concrete Electrical Resistivity. ACI Materials Journal, 119(6).

Hong, S. X., Lai, W. L., & Helmerich, R. (2012, June). Monitoring accelerated corrosion in chloride contaminated concrete with ground penetrating radar. In 2012 14th International Conference on Ground Penetrating Radar (GPR) (pp. 561-566). IEEE.

Hong, S., Lai, W. L., & Helmerich, R. (2015). Experimental monitoring of chloride-induced reinforcement corrosion and chloride contamination in concrete with ground-penetrating radar. Structure and infrastructure engineering, 11(1), 15-26.

Hu, M., Xu, Y., Li, S., & Lu, H. (2022). Detection of defect in ballastless track based on impact echo method combined with improved SAFT algorithm. Engineering Structures, 269, 114779.

Jafari, F., & Dorafshan, S. (2021). Bridge inspection and defect recognition with using impact echo data, probability, and Naive Bayes classifiers. Infrastructures, 6(9), 132.

Janku, M., Cikrle, P., Grosek, J., Anton, O., & Stryk, J. (2019). Comparison of infrared thermography, ground-penetrating radar and ultrasonic pulse echo for detecting delaminations in concrete bridges. Construction and Building Materials, 225, 1098-1111.

Jiao, L., Ye, Q., Cao, X., Huston, D., & Xia, T. (2020). Identifying concrete structure defects in GPR image. Measurement, 160, 107839.

Kee, S. H., Oh, T., Popovics, J. S., Arndt, R. W., & Zhu, J. (2012). Nondestructive bridge deck testing with air-coupled impact-echo and infrared thermography. Journal of Bridge Engineering, 17(6), 928-939.

Klimenko, Y. V., Kjlisnichenko, S. V., Polianskyi, K. V., & Popadenko, A. O. (2021). Possibility using thermographic control method to detect cracks in reinforced concrete structures.

Kot, P., Muradov, M., Gkantou, M., Kamaris, G. S., Hashim, K., & Yeboah, D. (2021). Recent advancements in non-destructive testing techniques for structural health monitoring. Applied Sciences, 11(6), 2750.

Kuruppu, K. A. B. P., Nanthakumar, M., & Baskaran, K. (2022, July). Study on Honeycombs in Structural Concrete Elements. In 2022 Moratuwa Engineering Research Conference (MERCon) (pp. 1-6). IEEE.

Lai, W. L., Kind, T., & Wiggenhauser, H. (2011). Using ground penetrating radar and time–frequency analysis to characterize construction materials. NDT & E International, 44(1), 111-120.

Lai, W. L., Kou, S. C., Tsang, W. F., & Poon, C. S. (2009). Characterization of concrete properties from dielectric properties using ground penetrating radar. Cement and Concrete Research, 39(8), 687-695.

Lai, W. L., Kind, T., Stoppel, M., & Wiggenhauser, H. (2013). Measurement of accelerated steel corrosion in concrete using ground-penetrating radar and a modified half-cell potential method. Journal of Infrastructure Systems, 19(2), 205-220.

Lai, W. W. L., Dérobert, X., & Annan, P. (2018). A review of Ground Penetrating Radar application in civil engineering: A 30-year journey from Locating and Testing to Imaging and Diagnosis. Ndt & E International, 96, 58-78.

Langman, A., & Inggs, M. R. (2001, July). Pulse versus stepped frequency continuous wave modulation for ground penetrating radar. In IGARSS 2001. Scanning the Present and Resolving the Future. Proceedings. IEEE 2001 International Geoscience and Remote Sensing Symposium (Cat. No. 01CH37217) (Vol. 3, pp. 1533-1535). IEEE.

Lee, C., Kee, S. H., Kang, J. W., Choi, B. J., & Lee, J. W. (2020). Interpretation of impact-echo testing data from a fire-damaged reinforced concrete slab using a discrete layered concrete damage model. Sensors, 20(20), 5838.

Lee, J. W., Lee, S. J., & Kee, S. H. (2021). Evaluation of a Concrete Slab Track with Debonding at the Interface between Track Concrete Layer and Hydraulically Stabilized Base Course Using Multi-Channel Impact-Echo Testing. Sensors, 21(21), 7091.

Luo, T. X., Lai, W. W., & Giannopoulos, A. (2020). Forward modelling on GPR responses of subsurface air voids. Tunnelling and Underground Space Technology, 103, 103521.

Matsuyama, K., Yamada, M., & Ohtsu, M. (2010). On-site measurement of delamination and surface crack in concrete structure by visualized NDT. Construction and Building Materials, 24(12), 2381-2387.

Nelson, T., Pham, L., Krauss, P., Wagner, E., Rahmani, E., & Dai, J. (2021). Bridge Deck Cracking Evaluation (No. FHWA-MT-21-005/9696-700).

Oikonomopoulou, E. C., Palieraki, V. A., Sfikas, I. P., & Trezos, C. G. (2022). Reliability and limitations of GPR for identifying objects embedded in concrete–Experience from the lab. Case Studies in Construction Materials, 16, e00898.

Park, J., Park, S., & Lim, Y. (2018). Application of Impact Echo Test Method to Detection of Separation Void between Layers of Concrete Slab Track Foundation. International Journal of Railway, 11(2), 39-44.

Perez Gracia, M. D. L. V. (2009, October). Resolution in evaluation of structural elements by using ground-penetrating radar. In Jornadas Técnicas Internacionales de Tecnologia de la Rehabilitación y Gestión del Patrimonio Construido (pp. 511-521).

Pospisil, K., Manychova, M., Stryk, J., Korenska, M., Matula, R., & Svoboda, V. (2021). Diagnostics of reinforcement conditions in concrete structures by GPR, impact-echo method and metal magnetic memory method. Remote Sensing, 13(5), 952.

Pratt, D., & Sansalone, M. (1992). Impact-echo signal interpretation using artificial intelligence. Materials journal, 89(2), 178-187.

Prego, F. J., Solla, M., Puente, I., & Arias, P. (2017). Efficient GPR data acquisition to detect underground pipes. NDT & E International, 91, 22-31.

Raju, R. K., Hasan, M. I., & Yazdani, N. (2018). Quantitative relationship involving reinforcing bar corrosion and ground-penetrating radar amplitude. ACI Materials Journal, 115(3), 449-457.

Sangoju, B., & Ramanjaneyulu, K. (2015). Estimation of rebar diameter in concrete structural elements using ground penetrating radar. NDE2015.

Sansalone, M., & Carino, N. J. (1989). Detecting delaminations in concrete slabs with and without overlays using the impact-echo method. Materials Journal, 86(2), 175-184.

Sansalone, M. J., & Streett, W. B. (1997). Impact-echo. Nondestructive evaluation of concrete and masonry.

Schubert, F., & Köhler, B. (2008). Ten lectures on impact-echo. Journal of Nondestructive Evaluation, 27, 5-21.

Sengupta, A., Ilgin Guler, S., & Shokouhi, P. (2021). Interpreting impact echo data to predict condition rating of concrete bridge decks: a machine-learning approach. Journal of Bridge Engineering, 26(8), 04021044.

Sensors & Software Inc. (12/27/2022). Glossary of GPR Terms. https://www.sensoft.ca/resources/glossary-of-gpr-terms-2-2/.

Sham, J. F., & Wallace, W. L. (2017, June). Diagnosis of reinforced concrete structures by Ground Penetrating Radar survey-case study. In 2017 9th International Workshop on Advanced Ground Penetrating Radar (IWAGPR) (pp. 1-6). IEEE.

Shaw, M. R., Millard, S. G., Molyneaux, T. C. K., Taylor, M. J., & Bungey, J. H. (2005). Location of steel reinforcement in concrete using ground penetrating radar and neural networks. Ndt & E International, 38(3), 203-212.

Sultan, A. A., & Washer, G. A. (2018). Comparison of two nondestructive evaluation technologies for the condition assessment of bridge decks. Transportation Research Record, 2672(41), 113-122.

Swanson, D. A. (2015). On the relationship among values of the same summary measure of error when used across multiple characteristics at the same point in time: an examination of MALPE and MAPE. Review of Economics and Finance, 5(1).

TEST, I. E. (2008). SYSTEM REFERENCE MANUAL 2008.

Tinkey, Y., & Olson, L. D. (2007). Sensitivity studies of grout defects in posttensioned bridge ducts using impact echo scanning method. Transportation research record, 2028(1), 154-162.

Tosti, F., & Ferrante, C. (2020). Using ground penetrating radar methods to investigate reinforced concrete structures. Surveys in Geophysics, 41(3), 485-530.

Trung, D.H.; Giang, N.V. and Van, N.T. 2018. The application of depth migration for processing GPR data. ES3 Web of Conferences. 35. https://doi.org/10.1051/e3sconf/20183503004.

Wong, C. P., & Subramaniam, R. (2019). Exploring thermal effects and behaviors of chemical substances using an infrared camera. Journal of Chemical Education, 96(10), 2339-2344.

Wong, T. W. P., Poon, C. S., & Lai, W. L. W. (2018, June). Laboratory validation of corrosion-induced delamination in concrete by ground penetrating radar. In 2018 17th International Conference on Ground Penetrating Radar (GPR) (pp. 1-6). IEEE.

Xiao, H., Qin, J., Ogai, H., & Jiang, X. (2015). A new standing-wave testing system for bridge structure nondestructive damage detection using electromagnetic wave. IEEJ Transactions on Electrical and Electronic Engineering, 10(2), 157-165.

Xu, Y., Yan, D., Zhu, W., & Zhou, Y. (2020). Study on the mechanical performance and interface damage of CRTS II slab track with debonding repairment. Construction and Building Materials, 257, 119600.

Yehia, S., Abudayyeh, O., Nabulsi, S., & Abdelqader, I. (2007). Detection of common defects in concrete bridge decks using nondestructive evaluation techniques. Journal of Bridge Engineering, 12(2), 215-225.

Yehia, S., Qaddoumi, N., Farrag, S., & Hamzeh, L. (2014). Investigation of concrete mix variations and environmental conditions on defect detection ability using GPR. NDT & e International, 65, 35-46.

Zanzi, L., & Arosio, D. (2013). Sensitivity and accuracy in rebar diameter measurements from dual-polarized GPR data. Construction and Building Materials, 48, 1293-1301.

Zein, A. S., & Gassman, S. L. (2010). Frequency spectrum analysis of impact-echo waveforms for t-beams. Journal of Bridge Engineering, 15(6), 705-714.

Zhu, S., Wang, M., Zhai, W., Cai, C., Zhao, C., Zeng, D., & Zhang, J. (2018). Mechanical property and damage evolution of concrete interface of ballastless track in high-speed railway: Experiment and simulation. Construction and Building Materials, 187, 460-473.

APPENDIX A

SETTINGS FOR THE MEASURING PRESETS OF GPR

(i) Measuring Mode: There are two modes available; Line Scan and Area Scan. In the GP app, the B-scan and C-scan display modes, as previously discussed in Section 3, are referred to as 'Line Scan' and 'Area Scan', respectively.

(ii) Resolution: The resolution of GPR relates to the ability to detect and distinguish between two separate targets as well as the smallest target that GPR can detect. This parameter can be set to either 'Max Depth' or 'Max Speed'. The wavelength of the signal determines the resolution; the narrower the wavelength, the higher the resolution and the smaller the targets that may be identified. The frequency of the GPR signal determines the wavelength size, with lower frequency antennas physically delivering a larger signal and higher frequency antennas physically transmitting a smaller signal. A high-frequency GPR antenna cannot view a deep target or layer. Since GP8000 generates modulated frequencies ranging from 200-4000 MHz the resolution for this inspection is set to 'Max Depth'.

(iii) Repetition Rate (scans/in): This value represents the number of scans per second that the system will store in its memory. There are three options: 1.25, 2.50, and 5.00 scans per horizontal distance unit (inches). Because the data was collected based on distance, the highest number, 5.00 scans/in, was selected. Although smaller scan spacing results in higher resolution data, previous studies recommended the densest scan spacing, such as 60 scans/foot or 5 scans/inch, for detecting shallow structural defects in concrete specimens [59].

(iv) Units: Imperial and Metric units are available; however, Imperial units were chosen for this study to avoid unnecessary conversion.

APPENDIX B

SETTINGS FOR THE IMAGE PROCESSING OF GPR

The image processing of GPR data in the system settings is governed by three distinct parameters: (i) Gain; the addition of signal to compensate for the natural effects of attenuation, (ii) Noise; potential interference from nearby signal emitters, and (iii) Dielectric Constant, Dk (ε_t); reflection coefficient at the interface of a material caused by propagation velocity of EM waves. Gain adjustments, on the other hand, can alter the radar signal and should be used with caution to avoid artifact development. When a gain function is applied to a noisy signal, the late-arrival noise components are amplified, which may result in incorrect data interpretation. Gain adjustment is recommended for image processing only when GPR data is made noise free or after a thorough de-cluttering. To avoid errors during data collection due to incoherence between gain adjustments and noise cancellations, all scans in this study were taken as a pre-set operation mode 'Auto Gain' and 'Noise Cancellation' by the GPR unit (probe). When this mode is selected, the system automatically selects the amplitude (gain) points when the antenna comes into contact with the examined surface, while the user selects only the penetration depth (in terms of distance) through Dk calibration.

[1]Trace: Point reading of GPR that indicate the time variation of signal amplitude.

[2]The Envelope: It is obtained by using the method referred to as the Hilbert transform to calculate the positive and negative traces; the positive bounding trace is normally referred to as 'the envelope'. The envelope can be formed from a pair of traces that uniquely bracket the extremes of an oscillatory signal. The signal is assumed to have a zero average or base line, so the upper and lower traces are identical but of opposite sign.

APPENDIX C

SETTINGS FOR THE DATA ACQUISITION PARAMETERS OF IE

The initial gain was set to 100 by default. As suggested by the manufacturer, this is assumed to be a good value for most IE tests. A time/point or sampling rate of 7 microsecond (uSec) was used and the record size (points per record time) for each waveform was set at 512 data points. Therefore, # Recs =2 was chosen as the total number of IE data records to save, which should be sufficient for the investigation of concrete slabs. The selection of impact source is one of the most important subjective data acquisition parameters. If the solenoid parameter (Sol.) is enabled, the system will use the solenoid in the IE head as a source. If this value is not set, the system will use an external source impactor (i.e., steel ball hammer). For this experimental program, 'Sol.' was set 'ON' and the time to drive the solenoid (Sol. Time) was kept at the default value of 14 us (microsecond). The maximum thickness for investigation was set at 6 inches for all four concrete specimens. The specified IE connector was used to connect the IE head to the NDE-360 platform. Therefore, only one channel, denoted by 'Ch 1' will be used for the IE data recording. For Ch 1, the transducer type must be set to 'Displacement'. This is due to the high propagation speed and amplitude of P-waves. Surface displacement caused by reflected wave arrivals is dominated by displacement caused by P-waves. In addition, the transducer calibrations (unit/volt) were set to the default value of 1. Here, 'unit' is the engineering unit (Metric or English) desired for the result on a given channel. To obtain accurate IE readings, Ch 1 must be activated prior to data recording, and the respective parameter settings must remain unchanged.